Spiking activity in the visual thalamus is coupled to pupil dynamics across temporal scales

Davide Crombie[1,2], Martin A. Spacek[1], Christian Leibold[1,3,*], and Laura Busse[1,4,*]

[1]Division of Neurobiology, Faculty of Biology, LMU Munich, Munich, Germany
[2]Graduate School of Systemic Neurosciences, LMU Munich, Munich, Germany
[3]Fakultät für Biologie & Bernstein Center Freiburg, Albert-Ludwigs-Universität Freiburg, Freiburg i. Br., Germany
[4]Bernstein Center for Computational Neuroscience, Munich, Germany
[*]Shared senior authors

Summary

The processing of sensory information, even at early processing stages, is influenced by the internal state of the animal. Internal states, such as arousal, are often characterized by relating neural activity to a single "level" of arousal, defined by a behavioral indicator such as pupil size. In this study, we expand the understanding of arousal-related modulations in sensory systems by uncovering nested timescales of pupil dynamics and their relationship to neural activity. Specifically, we observed coupling between spiking activity in the mouse dorsolateral geniculate nucleus (dLGN) of the thalamus and pupil dynamics across timescales spanning three orders of magnitude, from seconds to minutes. Throughout all of these timescales, two distinct spiking patterns – tonic spikes and bursts – preferred opposing phases of pupil dynamics. This phase-coupling could not be explained by pupil size *per se*, transitions between locomotion and quiescence, or saccadic eye movements. Furthermore, this phase coupling persisted even during viewing of a naturalistic movie, where it contributed to differences in how visual information was encoded. We conclude that dLGN spiking activity is simultaneously influenced by arousal processes associated with pupil dynamics across a broad range of timescales, with implications for the transfer of sensory information to the cortex.

Introduction

Information processing, even at the earliest sensory stages, is modulated by context. One prominent contextual effect is that of behavioral state or arousal, which has been shown to change neural activity throughout the brain [1–4]. Classic indicators for arousal are pupil size or its dynamics [5–8]. However, it is not well understood how the pupil signal is affected by the multitude of potential arousal-related factors, and, in turn, how the various influences on the pupil signal relate to spontaneous and stimulus driven neural activity.

An ideal system to investigate arousal-related modulations of neural activity is the visual thalamus, where neurons have long been known to display prominent patterns of activity associated with arousal [9–12]. In particular, two state-related firing modes have been described: burst firing, which is more prevalent during low-arousal states [9] and behavioral inactivity [12, 13]; and tonic firing, which is observed during alertness. Burst firing in the thalamus is characterized by a high frequency discharge of action potentials after sustained hyperpolarization, and it relies on the activation of low-threshold, transient calcium (T) channels [reviewed in 14]. In contrast, tonic firing

occurs when the membrane potential is relatively depolarized, and T-type calcium channels are inactivated [14]. Since thalamorecipient circuits in primary sensory cortices are highly sensitive to the temporal coordination of inputs [15–17], the presence of bursts and tonic firing can have different effects on postsynaptic cortical neurons [18]. This has led to the hypothesis that thalamic nuclei use burst and tonic firing modes to gate or alter the flow of information to and between cortical areas according to the arousal state of the animal [14].

While previous studies have often relied on a single variable to define the state of the animal, several lines of evidence suggest that arousal-related modulations of neuronal activity cannot be adequately characterized by assigning a single "level" of arousal to experimental epochs. For example, studies simultaneously measuring locomotion and pupil-linked arousal have revealed distinct effects in the visual cortex [6, 8]. More generally, a substantial fraction of shared variability present in large populations of neurons in visual cortex can be explained by high-dimensional sets of behaviors [19], indicating that the state of sensory systems at any given moment results from a combination of multiple processes [3]. One potential factor that distinguishes these processes is the timescale over which they extend. Externally, individual behaviors are organized into longer-lasting sequences and states [20]. Meanwhile, in the brain, a single arousal-related neuromodulator can have an impact across several timescales [21–24], and multiple neuromodulatory systems can influence neural activity over broadly different timescales [25].

To move beyond relating neural modulations to a single "level" of arousal, we here characterize modulations of spiking activity in the thalamic dorsolateral geniculate nucleus (dLGN) with respect to pupil size dynamics, taking into account the nested nature of arousal-related processes across different temporal scales. We discovered that both tonic and burst spiking in the dLGN were coupled to fluctuations in pupil size over timescales ranging from seconds to minutes. Across these timescales, tonic spikes preferred opposing phases of the pupil signal compared to bursts. These multi-scale influences on dLGN activity could not be explained by the pupil size *per se*, and could occur in the absence of changes in overt locomotion state. Furthermore, these modulations were not only present in the absence of a visual stimulus, but also were prevalent during presentations of naturalistic movies, despite the presence of rich stimulus-driven neural activity. Finally, we found that opposing phases of pupil dynamics across all timescales were associated with differences in the encoding of naturalistic movies by the dLGN, indicating that neural activity modulations coupled to the pupil size dynamics across various timescales contribute to state-dependent differences in the flow of sensory information to the cortex. Our findings support the notion that arousal-related modulation, rather than being a singular process, likely involves an interplay of changes occurring over diverse timescales.

Results

To assess how dLGN spiking activity is influenced by internal state, we paired extracellular silicon probe recordings with video-based analysis of pupil size. During these recordings, mice were head-fixed, but free to run on an air-cushioned styrofoam ball under largely iso-luminant conditions (Figure 1A). We measured pupil size and locomotion

speed as indicators of the internal and behavioral states of the animal. Pupil size, a marker for internal states such as arousal, was in continuous fluctuation throughout the recordings under constant illumination (see example in Figure 1B, black trace; Figure S1A, gray and pink distributions; N = 15 sessions in 10 mice). Similarly, active and quiescent behavioral states, as measured by locomotion (Figure 1B, green trace), were observed in all experiments. The proportion of time spent running varied across experiments, ranging from 0.1–0.47 (median = 0.22, Figure $S1B_{1-2}$). Consistent with previous studies [12, 26], bouts of locomotion were often accompanied by increases in pupil size (Figure $S1B_3$). However, we also noticed that similar ranges in pupil size fluctuations occurred within both active and quiescent behavioral states (Figure $S1B_3$). In accordance with previous results [6], this suggests that diverse internal states may coexist within a behavioral state.

We observed that fluctuations in pupil size during both locomotion and quiescence were accompanied by diverse changes in the spiking activity of dLGN neurons. For instance, the neuron shown in Figure 1B generally increased its firing rate when the pupil was large. To characterize the relationship between pupil size and firing rates, we fit a flexible class of modulated Poisson models to spike counts (binned in 250 ms windows). These models revealed that the relationship between pupil size and dLGN firing rate varied between neurons, and was often non-monotonic (Figure $1C_1$), reminiscent of previous observations in cortex [7]. Indeed, among the 89.7% of recorded dLGN neurons showing significant modulation across pupil size, the majority (53.6%) had their peak firing rate outside the top decile of pupil size. Across the recorded population of neurons, peak firing rates spanned the entire range of pupil sizes (Figure $1C_1$; N = 156 neurons). In addition to this diverse relationship, we found that, for the vast majority of neurons and pupil size bins, pupil size provided only limited information about firing rate: variance of firing rates within pupil size bins was high and in fact often larger than the mean (Wilcoxon rank-sum test for mean Fano factor > 1: $W = 431.0$, $p = 7.35\times10^{-21}$). There was also no systematic relationship between variance of firing rates and the predicted mean (Figure $1C_2$). Similar results were obtained in recordings conducted in darkness (Figure S1C), indicating that the overall relationship between pupil size and firing rate observed in our study mainly originates from non-visual factors, such as internal processes related to arousal. Returning to the raw data (Figure 1B), on top of the relationship to pupil size *per se*, we found clear instances where firing rate increases were coupled to dilating phases of the pupil dynamics (Figure 1B, 1). These dilation-related firing rate changes could occur while the pupil was relatively constricted (Figure 1B, 2), and could be of similar magnitude to those accompanying a relatively large pupil (Figure 1B, 3). We thus sought to develop a framework that could capture this breadth of modulations in dLGN spiking activity by focusing on the pupil dynamics.

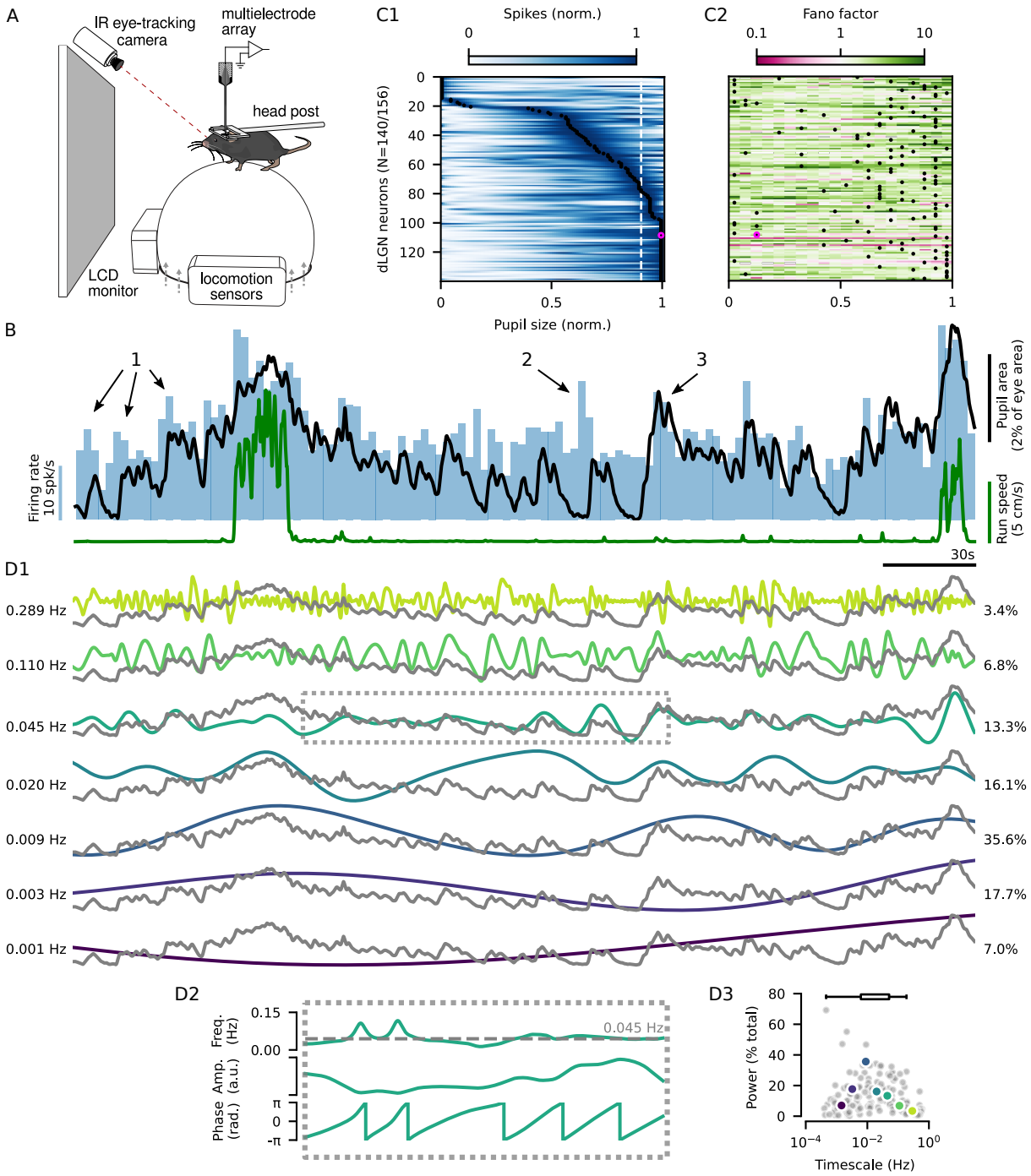

Figure 1 Extracellular recordings from the dLGN reveal diverse arousal-related modulations of firing rate. (A) Schematic of the experimental setup. **(B)** Pupil size (*black*) and running speed (*green*) overlaid on the firing rate from an example simultaneously recorded dLGN neuron (*blue*, binned in 2 s windows). **(C1)** A Poisson generalized additive model was fit to predict spike counts in 250 ms windows for each neuron based on pupil size. Predicted spike counts (min-max normalized) across pupil sizes (min-max normalized) are illustrated as a heatmap for all dLGN neurons with significant modulation (140/156; ANOVA $p \leq 0.05$). Neurons were sorted by the pupil size with the highest predicted spike count (*black dots*). The example neuron from (B) is shown in *magenta*. The *dashed white line* indicates the 90th percentile of pupil size. **(C2)** Fano factor (variance of spike counts / predicted mean) across pupil size bins, with the same sorting of neurons as in (C1). *Black dots* indicate the pupil size with the highest spike count variance for each neuron. **(D1)** The pupil size trace in (B) (*gray traces*) separated into components of pupil dynamics (CPDs) occurring over different timescales (*colored traces*). The components are described by their characteristic frequency (*left*) and power (% total, *right*). **(D2)** An illustration of how CPDs are characterized according to their frequency, amplitude and phase using the trace indicated by the *dashed box* in (D1). *Top*: The characteristic frequency (*grey dashed line*) is computed as the amplitude-weighted mean of the component's instantaneous frequency. *Middle*: The power is defined as fraction of total power density, computed from the squared amplitudes of all CPDs derived from the same pupil signal, contributed by the component. *Bottom*: The phase of the CPD describes if the pupil is undergoing dilation ($-\pi$ to 0) of constriction (0 to π) at the timescale defined by the component. **(D3)** The characteristic timescale of each CPD plotted against the power. Components from the example recording in (B, D) are shown in color. The inset box plot (*top*) shows the distribution of the components with the maximum power from each recording, highlighting the diversity of pupil dynamics.

To gain a better understanding of these modulations in dLGN firing rates, we explored the multi-scale dynamics of the pupil signal, aiming to extract information about changes in internal state beyond the size of the pupil *per se*. Indeed, previous studies dating to the beginning of pupillometry have suggested that a relevant indicator of arousal-related modulation can be the dynamics of the pupil [27–29]. The relationship between pupil dynamics and internal states has also been explored in mouse visual cortex [6], where associations between pupil dynamics and neuromodulatory signaling for both phasic and sustained pupil changes were observed [25]. Building on these studies, we observed that pupil size changes could be described over a variety of temporal scales [7]: from minutes-long changes sometimes associated with overt movement, to cycles of dilation and constriction lasting 10s of seconds, to very quick changes on the order of seconds. We therefore employed a data-driven approach, called empirical mode decomposition (EMD, see Methods), to split the pupil signal into components capturing its underlying dynamics across this broad range of temporal scales (Figure 1D). Each component of pupil dynamics (henceforth, CPD) is characterized by its temporal scale (Figure $1D_1$, left; Figure $1D_2$) and its relative power (Figure $1D_1$, right; Figure $1D_2$). The extracted CPDs spanned several orders of magnitude in temporal scale, capturing dilation-contraction cycles lasting from several minutes (10^{-3} Hz) to just a few seconds (10^0 Hz). Components with particularly high power were found across this entire range (Figure $1D_3$), substantiating the observed diversity of timescales present in pupil dynamics. Importantly, the set of components extracted from a single pupil trace exhibited only limited periods of phase synchronization (Figure S1D), indicating that dynamics at different timescales were largely independent of each other.

To characterize the relationship between dLGN activity and multi-scale pupil dynamics, we performed a phase coupling analysis relating the components of pupil dynamics to two types of dLGN spiking (Figure 2). We separated the spiking activity from each dLGN neuron into tonic spiking and bursting (bursting was defined by $\geq$100 ms with no activity followed by $\geq$2 spikes with $\leq$4 ms ISI [30]; Figure 2A). Consistent with previous findings in awake animals, we found that bursts occurred at a much lower rate than tonic spikes, and accounted for only 3% of spikes on average (median burst ratio for the 95% of neurons with bursting, Figure $S2A_2$). Despite their small contribution to the total spike count Figure $S2A_1$, bursts provide an important extracellular marker for the membrane potential status of thalamic neurons. Bursts additionally play an important role in determination of rhythmic cortical states [13]. Indeed, we found that the mean auto-correlogram of bursts had a peak at $\sim$0.2 s, indicating rhythmic occurrence at $\sim$5 Hz (Figure $S2B_2$), while the zero-centred peak in the mean burst cross-correlogram indicated that bursts tended to occur synchronously between neurons (Figure S2C). After separating burst and tonic spikes, for each neuron and simultaneously recorded CPD, we then performed a phase coupling analysis, collecting the phase of the CPD at the time of bursts – considering all spikes in the burst as one single event – or tonic spikes (Figure 2B). Taking the circular mean angle of these collected phases allowed us to determine the preferred phase of spiking. To quantify the strength of phase coupling, we used the bias-corrected squared circular mean length [31], which allowed comparisons between neurons with different firing rates and between bursting and tonic spiking. Finally, to

evaluate the significance of the phase coupling, we compared the observed coupling strength to a null-distribution of coupling strengths obtained from surrogate spike trains to account for the presence of short timescale spike patterns ($\leq$ 300 ms; Figure S2B$_1$, Figure S2B$_2$), as these patterns could potentially inflate coupling strengths.

We found that both tonic spiking and bursts in dLGN neurons were coupled to pupil dynamics across a wide range of temporal scales (Figure 2C). Significant coupling of to at least one component of pupil dynamics was measured in 96.8% (153/158) of dLGN neurons for tonic spiking, and 86.5% (109/126) for bursting. Examining the phase coupling for all neurons and simultaneously recorded CPDs (Figure 2C), we found that this coupling was not limited to a single temporal scale, but rather occurred over time scales spanning seconds to several minutes ($1-0.001$ Hz). Across all these time scales, bursts were coupled to a phase opposing that of tonic spiking (Figure 2D, V-test for non-uniform distribution with a mean of π: V = 140.7, p = 0.0). The coupling strengths for both tonic spiking and bursting were dependent on the temporal scale (Kruskal-Wallis one-way ANOVA for tonic spiking: H = 66.4, p = 5.8×10^{-13}; bursting: H = 32.1, p = 5.8×10^{-6}), but bursting consistently displayed stronger coupling than tonic spiking (Figure 2E; Wilcoxon rank-sum test with coupling strengths pooled across timescales: W = 3.3×10^{3}, p = 2.0×10^{-33}), suggesting that burst spike may be a more exclusive indicator of the internal state of dLGN neurons. The same analyses performed on data collected in darkness also revealed significant phase coupling across temporal scales (significant coupling observed for at least one timescale and spike type in 95.7% of neurons; Figure S3A), indicating that coupling to CPDs is likely driven by changes in internal state rather than visual stimulation. Furthermore, the phase relationship between bursting and tonic spiking was largely preserved (Figure S3A$_2$), and, although coupling strengths in darkness were marginally weaker, the strength relationship between bursting and tonic spiking was also preserved (Figure S3A$_3$). Together, these results support the notion that dLGN neurons undergo modulations driven by internal factors linked to pupil dynamics across a broad range of temporal scales.

Next, we asked whether the modulations we observed across multiple temporal scales resulted from different neurons being modulated at different time scales, or if nested modulations were present within the spiking of single neurons. Our analysis revealed that, both for bursts and tonic spiking, many neurons showed modulations at more than one temporal scale (Figure 2F). While tonic spiking had a tendency towards multi-scale modulation, with a higher proportion of neurons being coupled to $>$1 CPDs, bursting was more likely to be modulated at a single temporal scale (Figure 2F; mean number of timescales for tonic spiking: 4.32, mean number of timescales for bursting: 2.49). Among neurons with multi-scale coupling, there was no overwhelmingly dominant temporal scale of modulation, indicated by a gradual decay in coupling strengths from the strongest to the weakest (Figure S3C$_1$). To ensure that potential phase relationships between the CPDs (Figure S1E) were not underlying the observed coupling to multiple temporal scales, we repeated the phase coupling analysis after removing periods of time in which the components themselves might be coupled (Figure S3B). Coupling strengths across timescales remained unchanged for both bursts and tonic spikes (Figure S3B$_3$; Mann-Whitney-U test for each timescale, all p-values $>$0.05), and

the majority of neurons retained their coupling to more than one temporal scale (Figure S3B$_4$). Turning back to analyses performed on the the full dataset (Figure 2), the specific timescale to which a neuron was most strongly coupled varied greatly between neurons, covering almost the entire range of observed coupling timescales (Figure S3C$_1$). Notably, part of this variability could be attributed to the mouse and/or recording session (Figure S3C$_2$, Figure S3C$_3$), potentially reflecting session-specific differences in overt behavior. However, in almost all recording sessions, we found the preferred timescale of neurons from the same recording was distributed across more than one component (tonic: 15/15 sessions, burst 13/15 sessions; Figure S2C$_2$, Figure S2C$_3$). This suggests that the timescale of strongest modulation is not only influenced by factors common to the recording session, but also by neuron-specific factors. We thus conclude that the spiking activity of individual dLGN neurons can be coupled to pupil dynamics across multiple independent temporal scales, and that neurons are most strongly coupled to a diversity of timescales.

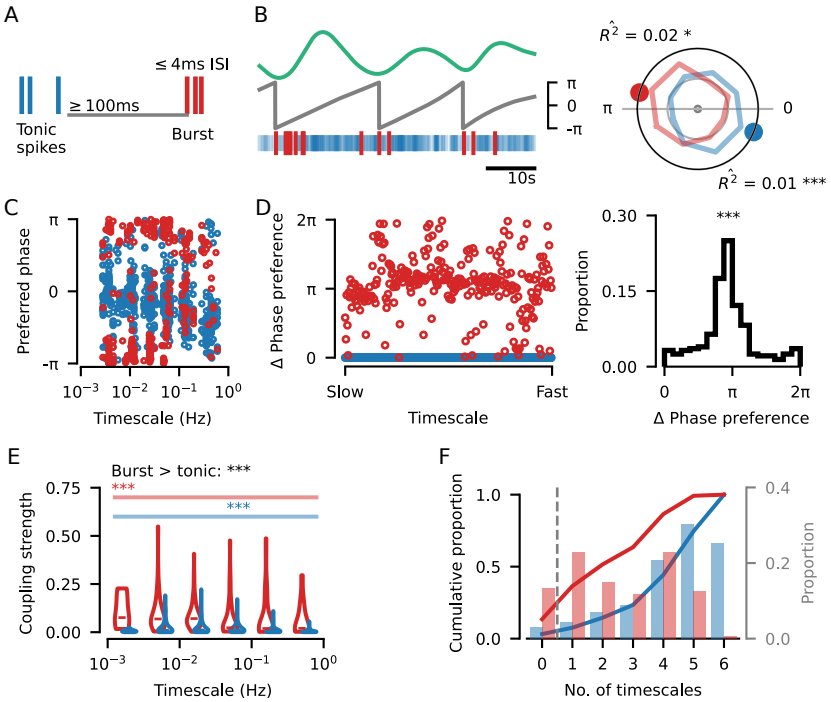

Figure 2 Tonic spikes and bursts in the dLGN are coupled to pupil dynamics across multiple timescales. (A) Bursts (*red*) were defined as ≥ 2 spikes occurring after > 100 ms of silence and with an inter-spike interval less than 4 ms [30], all remaining spikes were classified as tonic spikes (*blue*). For the phase coupling analysis below, all spikes in a burst were treated as a single burst event. **(B)** *Top*: example component of pupil dynamics (CPD). *Middle*: the corresponding phases of the example CPD. *Bottom*: simultaneously recorded tonic spiking (*blue*) and bursting (*red*) from an example neuron. *Right*: the phase distributions for bursts and tonic spikes from the example neuron-CPD pair ($\hat{R}^2$: coupling strength; *colored dots*: preferred phase). Significant coupling to a CPD (*asterisks*, * for p≤0.05, ** for p≤0.01, *** for p≤0.001; see Methods) indicates that the activity of the neuron undergoes modulation that is tracked by pupil dynamics with a certain temporal scale. **(C)** The preferred coupling phase of bursts and tonic spikes for all neuron-CPD pairs with significant coupling. Significant burst or tonic spike coupling to at least one CPD was observed in 94.4% of neurons (153/162). **(D)** Burst - tonic spike phase differences for each neuron-component pair in (C) with significant coupling for both types of spiking across timescales (*left*). The overall distribution (*right*) was centered around 2.8 radians (V-test for non-uniform distribution with a mean of π: V = 140.7, p = 0.0), showing that bursts and tonic spikes preferred opposing phases of pupil dynamics regardless of the temporal scale. **(E)** Coupling strength distributions for all significantly coupled neuron-CPD pairs binned by the timescale (*small horizontal bars*: median coupling strength; *blue horizontal bar*: Kruskal-Wallis one-way ANOVA across timescales for tonic spike coupling strengths, H = 66.4, p = 5.8×10^{-13}; *red horizontal bar*: Kruskal-Wallis one-way ANOVA across timescales for burst coupling strengths, H = 32.1, p = 5.8×10^{-6}; *asterisks* centered on timescale with the highest median coupling strength; *burst > tonic*: Wilcoxon rank-sum test pooling across timescales, W = 3.3×10^3, p = 2.0×10^{-33}). **(F)** Cumulative distribution of the number of CPDs to which each neuron was coupled. *Faded bars* show the underlying proportions on the right y-axis. Although more neurons were only coupled to a single component with respect to bursting, the majority of neurons were coupled to more than one CPD, indicating that their spiking activity reflected more than one independent timescale of modulation.

Our phase coupling framework allows us to capture modulations that are associated with aspects of the pupil signal other than pupil size *per se*; however, there are instances when coupling to pupil size can coincide with CPD phase coupling. Inspecting the example neuron and CPDs in Figure 1, for instance, it becomes apparent that peaks and troughs of certain components may coincide with large and small pupil sizes. To disentangle the influence of pupil size from phase coupling, we minimized differences in the distributions of pupil sizes between the phases of each CPD by sub-sampling time periods from the recordings (Figure 3A$_1$, see Methods). We then assessed phase coupling considering only the spikes that occurred in these sub-sampled periods, noting that, especially for slower CPDs, only a small proportion of the original data could be retained for analysis (Figure 3A$_2$). Despite this reduction, we found that coupling of bursting and tonic spiking to CPDs was largely retained (tonic spikes: 94.5% of neurons had coupling to at least one CPD; bursts: 59.0% of neurons; Figure 3B$_1$, Figure 3C$_2$). The

characteristic opposing phase preferences of bursts and tonic spikes in the same unit was also retained (V-test for non-uniformity and a mean of π: $V = 20.4$, $p = 9.5 \times 10^{-4}$). Although individual neurons displayed coupling to fewer number of timescales after sub-sampling (Figure $3B_1$), we observed that these losses primarily occurred at slower timescales (Figure $3B_2$), where only a small amount of data remained after sub-sampling (Figure $3A_2$). This suggests that the decrease in coupling may be attributed to limited statistical power rather than a genuine lack of coupling. Overall, coupling strengths decreased for both bursts (Figure $3C_1$, top; Mann-Whitney-U test: $U = 1.5 \times 10^4$, $p = 3.3 \times 10^{-4}$), and tonic spikes (Figure $3C_1$ bottom; Mann-Whitney-U test: $U = 1.4 \times 10^5$, $p = 4.0 \times 10^{-7}$). When examining individual neurons, we found that many neurons shifted the timescale to which they were most strongly coupled (tonic spikes: 55.9%; bursts: 28.6%; Figure $3C_2$, faded colored slices). Strikingly, we found a sizeable proportion of neurons where the strongest coupling increased after controlling for pupil size (tonic spikes: 25.5%; bursts: 14.3%; Figure $3C_2$, popped-out slices), suggesting that for these neurons the effects of pupil size changes were masking other firing rate modulations related to pupil dynamics. We conclude that the majority of neurons undergo multi-scale modulations of bursting and tonic spiking that cannot be explained by pupil size *per-se*.

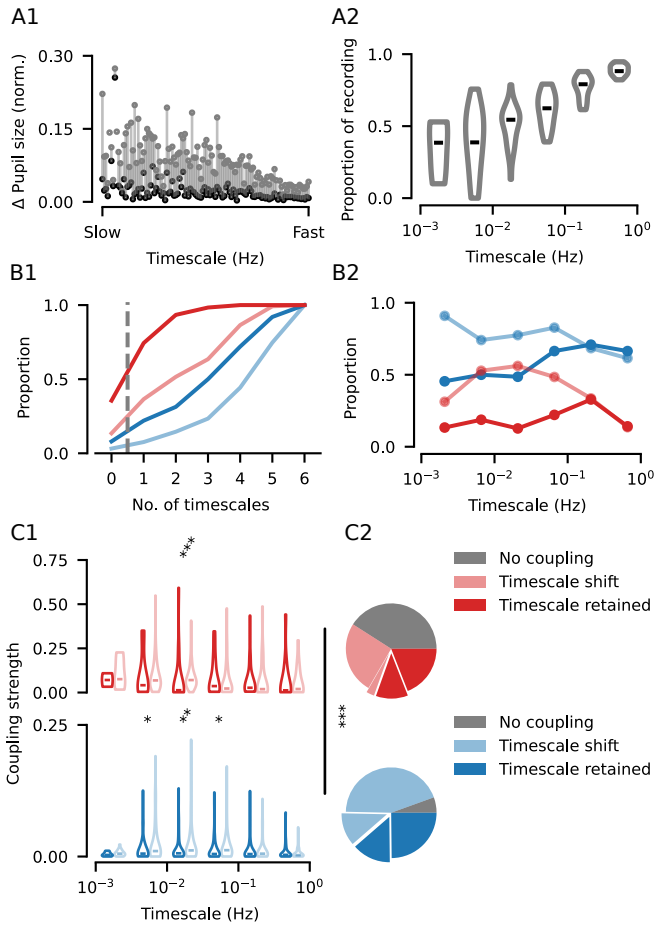

Figure 3 Coupling of dLGN spiking to pupil dynamics persists after controlling for pupil size. (A1) Comparison of the difference in pupil size (min-max normalized) between the phase bins from each CPD before (*grey*) and after sub-sampling (*black*), illustrating the efficacy of the size matching procedure. **(A2)** Proportion of the recording retained for analysis after the sub-sampling matching procedure for each timescale bin (*black bars*: median proportion). **(B1)** Cumulative distribution of the number of CPDs to which a neuron is significantly coupled. *Bold lines*: coupling measured only with spiking from recording periods matched for pupil size. *Faded lines*: coupling measured from full recording, same as in Figure 2F. **(B2)** The proportion of CPD-neuron pairs at each timescale with significant coupling, before (*faded lines*) and after (*bold line*) matching pupil size distributions. Note that the largest decreases after matching are for slower timescales where much less data was included (Figure 3A2), suggesting that these statistical tests may be under-powered. **(C1)** Coupling strength distributions before (*faded distributions*, Figure 2E) and after (*bold distributions*) controlling for pupil size (Mann-Whitney-U test for each timescale, p-value denoted by *asterisks*, * for $p \leq 0.05$, ** for $p \leq 0.01$, *** for $p \leq 0.001$) for bursts (*red, top*) and tonic spikes (*blue, bottom*). After controlling for pupil size bursts still have overall stronger coupling strength than tonic spikes (*vertical line, asterisks*: Wilcoxon rank-sum test for burst > tonic pooling across timescales). **(C2)** Proportion of neurons with significant phase coupling in Figure 2 that kept the same strongest modulation timescale (*bold slices*), shifted their strongest modulation timescale (*faded slices*), or completely lost their coupling (*gray slices*). The *highlighted slices* show the proportion of neurons that had an increase in coupling strength after controlling for pupil size.

We next investigated whether coupling between dLGN spiking and pupil size dynamics could be attributed to modulations driven by transitions in behavioral states. Previous studies have shown that changes in behavior, such as the transition from quiescence to locomotion, are accompanied by increased firing rates and decreased bursting in dLGN neurons [12, 32, 33]. Consistent with these findings, we observed a decrease in tonic spiking in a 5 s window surrounding the offset of a running bout (Figure S4A$_1$, see also [8]), and a sharp increase in tonic spiking, preceded by a slight decrease in bursting, in a 4 s window surrounding the onset of a running bout (Figure S4A$_2$). Periods of locomotion were also associated with an increased pupil size (Figure S1B$_3$). Unsurprisingly then, several CPDs were positively correlated to locomotion speed (54.3% of components with $p \leq 0.05$ in a permutation test;

Figure S4B$_1$, although note that the magnitude of the correlations is small). Given these findings, we asked if the CPD-linked spiking modulations we observed might be driven by these locomotion-correlated components. As a first step, we compared phase coupling across components, and observed that significant coupling in neuron-CPD pairs was equally likely regardless of whether the component was correlated to locomotion or uncorrelated (tonic spikes: correlated 93%, uncorrelated 91%, $\chi^2 = 0.58$, p = 0.44; bursts: correlated 78%, uncorrelated 81%, $\chi^2 = 1.18$, p = 0.27).

To explicitly remove the influence of behavioral state changes on the coupling between pupil dynamics and spiking activity, we computed the phase coupling taking into account only the spiking activity that occurred within a given behavioral state. We also excluded spiking activity in the transitional windows between behavioral states (Figure S4A; sit to run: -2 to 2 s; run to sit: -2 to 4 s). We first focused on periods of quiescence, which constituted on average 77% of the recordings (median proportion of time outside of running bouts; Figure S1B$_1$). During these quiescent periods, where variance in locomotion speed was low (Figure 4A$_1$), we found that the coupling between spiking activity and pupil dynamics was largely the same as when measured across the entire recording (Figure 4A$_2$). Neurons retained the anti-phase relationship between tonic spiking and bursting (Figure 4A$_3$; V-test for non-uniform distribution with a mean of π: V = 112.0, p = 0.0), with coupling to multiple timescales of pupil dynamics (Figure 4A$_4$), and similar coupling strengths across all timescales compared to the coupling measured across the whole recording (Figure 4A$_5$; Mann-Whitney-U test for tonic spike coupling strengths pooling across timescales: U = 2.2×10^5, p = $2.7\times10^{-}$; Mann-Whitney-U test for burst spike coupling strengths pooling across timescales: U = 4.3×10^4, p = 0.3).

Having shown that phase coupling across timescales persisted when measured only during periods of quiescence, we next repeated the same analyses focusing on periods with locomotion bouts (Figure 4B$_1$) and found similar coupling characteristics as for the other states. Tonics spikes and bursts showed preferences for opposing phases (Figure 4B$_2$ & B$_3$; V-test for non-uniform distribution with a mean of π: V = 25.8, p = 2.7×10^{-7}), while bursts were more strongly tuned than tonic spikes (Figure 4B$_3$; Wilcoxon rank-sum test pooling across timescales: W = 402.0, p = 5.5×10^{-3}). Although neurons were tuned to fewer temporal scales during locomotion (Figure 4B$_4$, there was a notable increase in coupling strengths (Figure 4B$_5$; Mann-Whitney-U test for tonic spike coupling strengths: U = 1.7×10^5, p = 2.6×10^{-32}; Mann-Whitney-U test for burst coupling strengths: U = 2.1×10^4, p = 5.6×10^{-8}). This was especially true of tonic spiking, such that the difference in coupling strength between tonic spikes and bursts was greatly reduced during locomotion. Given the higher behavioral variability during running bouts (Figure 4B$_1$), we hypothesized that particularly strong dLGN modulation in this state might be linked to changes in overt behavior, i.e. running speed. We therefore identified CPDs that were correlated to locomotion speed only *within* bouts of running (64.9% of CPDs; Figure S3C). Consistent with this hypothesis, we found that the running-correlated components were marginally more likely to drive significant phase coupling for bursts (correlated 82%, uncorrelated 74%, $\chi^2 = 4.64$, p = 0.03). Furthermore, running-correlated components had slightly higher coupling strengths

(Mann-Whitney-U for bursts: correlated median 6.3×10^{-2}, uncorrelated median 3.9×10^{-2}, U = 9.27×10^{3}, p = 0.02; Mann-Whitney-U for tonic spikes: correlated median 9.3×10^{-3}, uncorrelated median 6.1×10^{-2} U = 4.58×10^{4}, p = 0.06).

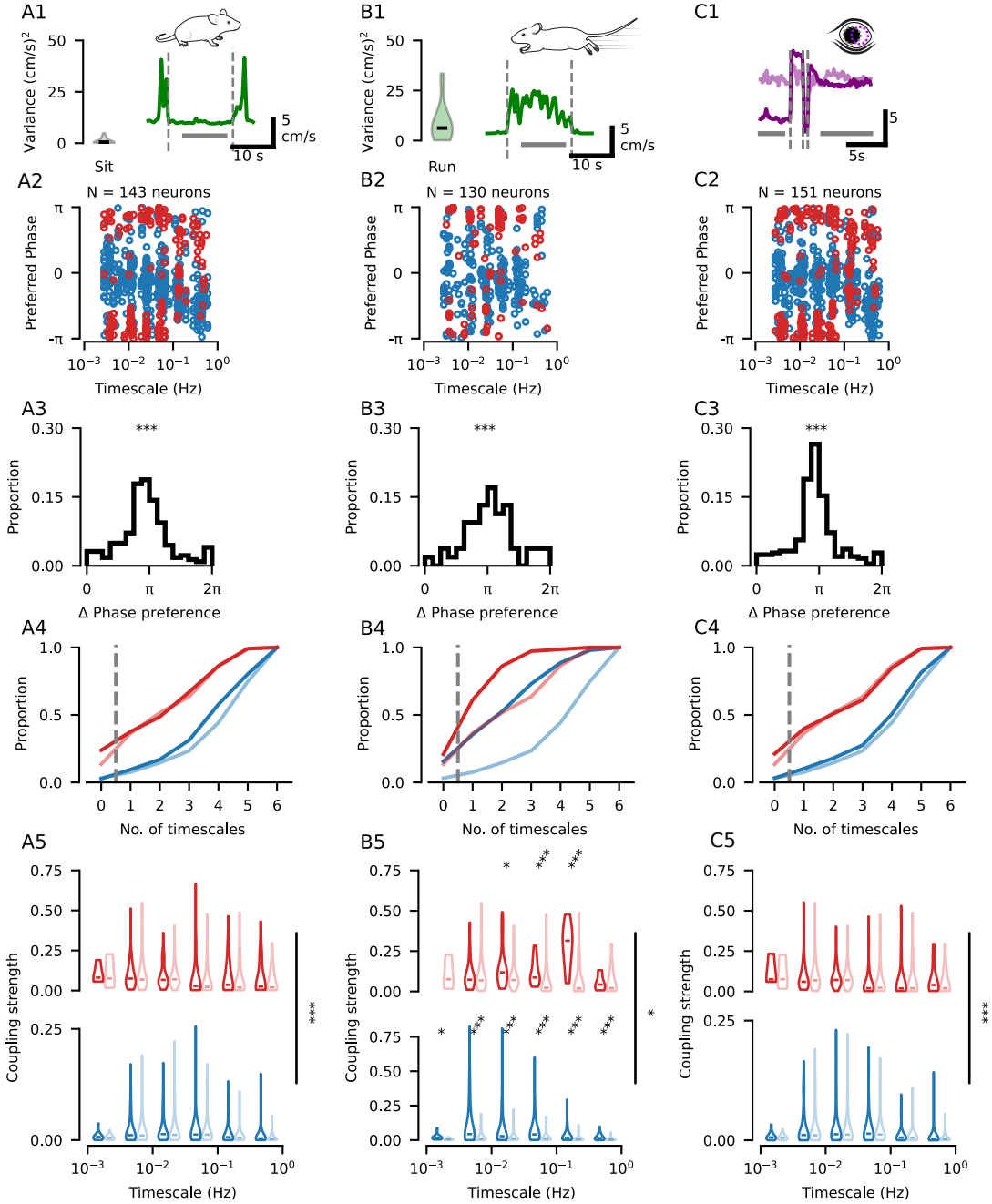

Figure 4 The coupling between dLGN spiking and pupil dynamics is not driven by overt behaviors. (A1) *Left*: the distribution of running-speed variance during quiescence across experiments (N = 14 experiments; *horizontal line*: median variance = 0.5 $(cm/s)^2$). *Right*: Locomotion speed for an example period of quiescence. *Dashed lines*: onset and offset of running bouts. *Gray bar*: period during which spikes were taken for the phase coupling analysis. Note that the 4 s after the offset of the first running bout and 2 s prior to the next running bout were not included in this time window. **(A2)** Timescale - phase relationship between spiking activity and pupil size dynamics as in Figure 2C, but computed using only spikes occurring during periods of quiescence. **(A3)** Difference in the preferred phase of bursts and tonic spikes across temporal scales for each neuron-component pair in (A2). **(A4)** Cumulative distribution of the number of coupling timescales for each neuron. *Faded lines*: the distribution when all spikes were considered (Figure 2F). *Bold lines*: the distribution when only spikes occurring during quiescence were considered. **(A5)** Coupling strengths across temporal scales for all neuron-component pairs in (A2) (*bold distributions*: coupling strengths during quiescence; *faded distributions*: coupling strengths from Figure 2E; Mann-Whitney-U test at each timescale, p-value denoted by *asterisks*, * for $p \leq 0.05$, ** for $p \leq 0.01$, *** for $p \leq 0.001$; *vertical line, asterisks*: Wilcoxon rank-sum test for burst > tonic pooling across timescales). **(B1)** *Right*: the distribution of running-speed variance during running bouts across experiments. (N = 14 experiments; *horizontal line*: median variance = 6.3 $(cm/s)^2$). *Left*: Locomotion speed for an example running bout. *Gray bar*: period during which spikes were taken for the phase coupling analysis. Note that the first and final 2 s of the running bout were not included in this time window. **(B2-5)** Same as (A2-5) but for spiking activity during locomotion bouts. **(C1)** Eye position for an example recording period with saccadic eye movements (*dark purple*: azimuth; *light purple*: elevation). *Gray bars*: the time windows without saccades during which spikes were taken for the phase coupling analyses (the -1 to 3 s of activity surrounding each saccade was excluded). **(C2-5)** Same as (A2-5) but after eliminating peri-saccadic spiking activity.

Apart from locomotion, other behaviors, such as eye movements, may also be associated with arousal and can induce changes in spiking activity. Indeed, upon visual inspection of eye position data, we noticed that saccades tended to occur during the dilation phase of large, slow pupil fluctuations, but also appeared to be related to smaller, faster fluctuations (Figure S5A). This observation resembled the relationship between tonic spiking and pupil dynamics (Figure 2C). To explore this further, we performed the same phase coupling analysis for saccades as we did for spiking, and found that saccades had an almost identical phase coupling profile to that of tonic spikes: saccades predominantly occurred during the dilating phases of multiple temporal scales of pupil dynamics (Figure S5B). To further investigate this relationship, we next asked if saccades could drive changes in spiking activity. Consistent with previous findings [reviewed in 34], we observed that bursting and tonic spiking in dLGN neurons was modulated in a short timescale window surrounding saccades. In a 4 s window surrounding saccades tonic spiking increased and bursting decreased, with the exception of a brief increase at the time of the saccade (Figure S5C_1). With regards to tonic spiking, neurons displayed diverse peri-saccadic activity patterns, amongst which we identified at least two distinct response types (Figure S5C_2). Despite this diversity, the overall effect of this modulation was an increase in tonic spiking in 88.0% of saccade-responsive neurons, while there was no consistent effect observed for bursting (Figure S4C_3). Thus, the overall effect of saccades on tonic spiking is similar to that of pupil dynamics.

We therefore hypothesized that the increase in spiking activity during the peri-saccadic period might contribute to the observed coupling between tonic spiking and pupil dynamics. We reasoned that, if the peri-saccadic increase in spiking was driving the coupling between tonic spikes and pupil dynamics, then coupling strengths and saccadic modulation strengths should be correlated. Indeed, we found that saccadic modulation strengths (Figure S5C3) were correlated with coupling strengths, but only for slower timescales of pupil dynamics, whereas the correlation was absent for faster timescales (Figure S5D). This pattern of results suggests that saccade rates and firing rates might be similarly co-modulated over timescales of minutes, but that the relatively rapid peri-saccadic modulation of spiking isn't related to neuron-CPD coupling. To completely eliminate the effect of saccade-driven changes in

spiking activity, similar to our approach for locomotion, we excluded spiking activity associated in a window from -1 s to 2 s surrounding saccades (Figure S5C1), and repeated the phase coupling analysis between tonic spikes / bursts and CPDs. We found that the main characteristics of the coupling between spiking activity and pupil dynamics were preserved across temporal scales, even without peri-saccadic activity. Neurons maintained their phase preference for tonic spikes and bursts (Figure $4C_2$; 93.2% of neurons had significant coupling to at least one CPD for either bursts or tonic spikes), their anti-phase relationship (Figure $4C_3$, V-test for non-uniform distribution with a mean of π: V = 144.0, p = 0.0) for multiple timescales (Figure $4C_4$), as well as their coupling strengths (Figure $4C_5$). We therefore conclude that, although behaviors like running and eye movements are reflected in some components of pupil size dynamics (Figure S3B-C; Figure S5A-B), and can induce changes in spiking (Figure S3A; Figure S4C), the coupling between spiking activity and pupil dynamics is likely additionally driven by internal factors that are distinct from these external behavioral states.

So far, we reported a multi-faceted coupling of dLGN activity to pupil dynamics in the absence of a patterned visual stimulus, but how stable is this coupling in the presence of a rich visual stimulus? At least two factors could potentially disrupt this coupling. Firstly, naturalistic stimuli have been shown to elicit repeated patterns of both tonic and burst firing in the dLGN [33, 35], which may dominate internally-driven activity fluctuations. Secondly, luminance changes or other salient features of the stimulus could induce pupil size changes that might interfere with those driven by internal state fluctuations. To address these issues, we presented five second-long naturalistic movie clips to mice while recording pupil size and dLGN activity (Figure 5; data from [33]). We observed that many neurons in the dLGN responded to the movies with regular patterns of activity, as exemplified by the neuron shown in Figure $5A_1$. However, the average response to the stimulus ("signal", Figure $5A_1$, bottom) often appeared weaker than the trial-to-trial variability in the time-averaged mean firing rates ("noise", Figure $5A_1$, right). We quantified this difference using the signal-to-noise ratio (SNR) of the stimulus responses (see Methods), and discovered that 100% of neurons had an SNR below 1 (Figure $5A_2$). In fact, for 90.6% of neurons, the noise was more than twice as strong as the signal (SNR < 0.5; Figure $5A_2$), indicating that dLGN neurons showed considerable variability in their responses that could not be accounted for by the visual stimulus. Similarly, when we repeated the same analysis for pupil size (Figure $5B_1$), we found that the movies did not systematically drive pupil size changes (Figure $5B_1$), resulting in an overwhelming dominance of trial-to-trial variance in pupil size (Figure $5B_2$). Thus, internally driven pupil dynamics remain largely uninterrupted by the naturalistic movie we presented. The analyses above suggest that factors unrelated to the stimulus, such as coupling to arousal-related variables, may be prevalent despite the prominent spiking responses evoked by the movie stimulus.

To investigate the coupling of spiking activity to pupil dynamics during naturalistic stimulus viewing, we decomposed the pupil size signal as before and characterized the phase coupling of bursts and tonic spikes. We found that neurons had similar coupling characteristics as in the absence of a patterned stimulus. Specifically, neurons were coupled to pupil dynamics across multiple timescales, with bursts and tonic spikes tending to preferring opposing

phases of dilation and contraction (Figure $5C_1$) and bursts displaying stronger coupling than tonic spikes (Figure $5C_2$). Furthermore, many individual neurons were simultaneously tuned to more than one timescale (Figure $5C_2$). Perhaps unsurprisingly, however, coupling strengths were generally decreased as compared to the conditions without a patterned stimulus (Figure $5C_3$, faded lines). To examine the implications of these findings for the encoding of arousal-related variables by dLGN spiking activity, we leveraged the repeating patterns of activity induced by the stimulus and next asked if pupil dynamics could be decoded from patterns of spiking activity. We first split each 5 s trial into 1 s segments, and, for each CPD, used the mean phase during each segment to assign one of two phase labels. We then used spiking activity from each individual neuron with significant phase coupling to decode the phase label. We found that the phase labels could be decoded above chance level for every timescale of pupil dynamics, both when using tonic spikes (Figure S6A) or bursts (Figure S6B). Together, these results show that dLGN neurons also represent multi-scale aspects of arousal during encoding of a naturalistic visual stimulus.

Given the different stimulus-response function of bursts and tonic spikes [35–37], we next asked whether the movie stimulus is differently represented by spiking activity during different phases of pupil dynamics. To this end, we used spiking activity to decode which of the five 1 s stimulus segments was presented (Figure 5D). For each CPD-neuron pair, we sorted the stimulus segments into two groups, according to the phase of the component at the time when the segment was on screen (Figure $5D_1$). These two phase groupings were designed such that one phase bin was centered on the preferred phase of tonic spiking, while the other phase bin was centered 180°opposite. Critically, we used all spikes to decode the identity of the stimulus segment, regardless of whether they were tonic spikes or part of a burst, to simulate the perspective of a downstream structure like the cortex that would be blind to this classification.

We observed that decoders trained and tested on data from the same phase group (Figure $5D_2$) achieved nearly perfect performance (Figure $5D_3$), indicating that spiking activity during either phase was informative about the stimulus segment. However, when we tested the decoder trained using spiking activity from one phase group with activity occurring during the opposite phase grouping (Figure $5E_1$), we found a marked decrease in decoding performance (Figure $5E_3$). Critically, this decoding penalty was only considered significant if it was greater than the penalties obtained by performing the same cross-group decoding analysis on random partitions of the data (Figure $5E_2$). The overall negative decoding penalty implies that encoding of the stimulus into firing rates differs between the phases of pupil dynamics. Importantly, this was not limited to a specific temporal scale of pupil dynamics, but was observed across the entire range of timescales examined, indicating that multiple temporal scales of modulation affect stimulus encoding.

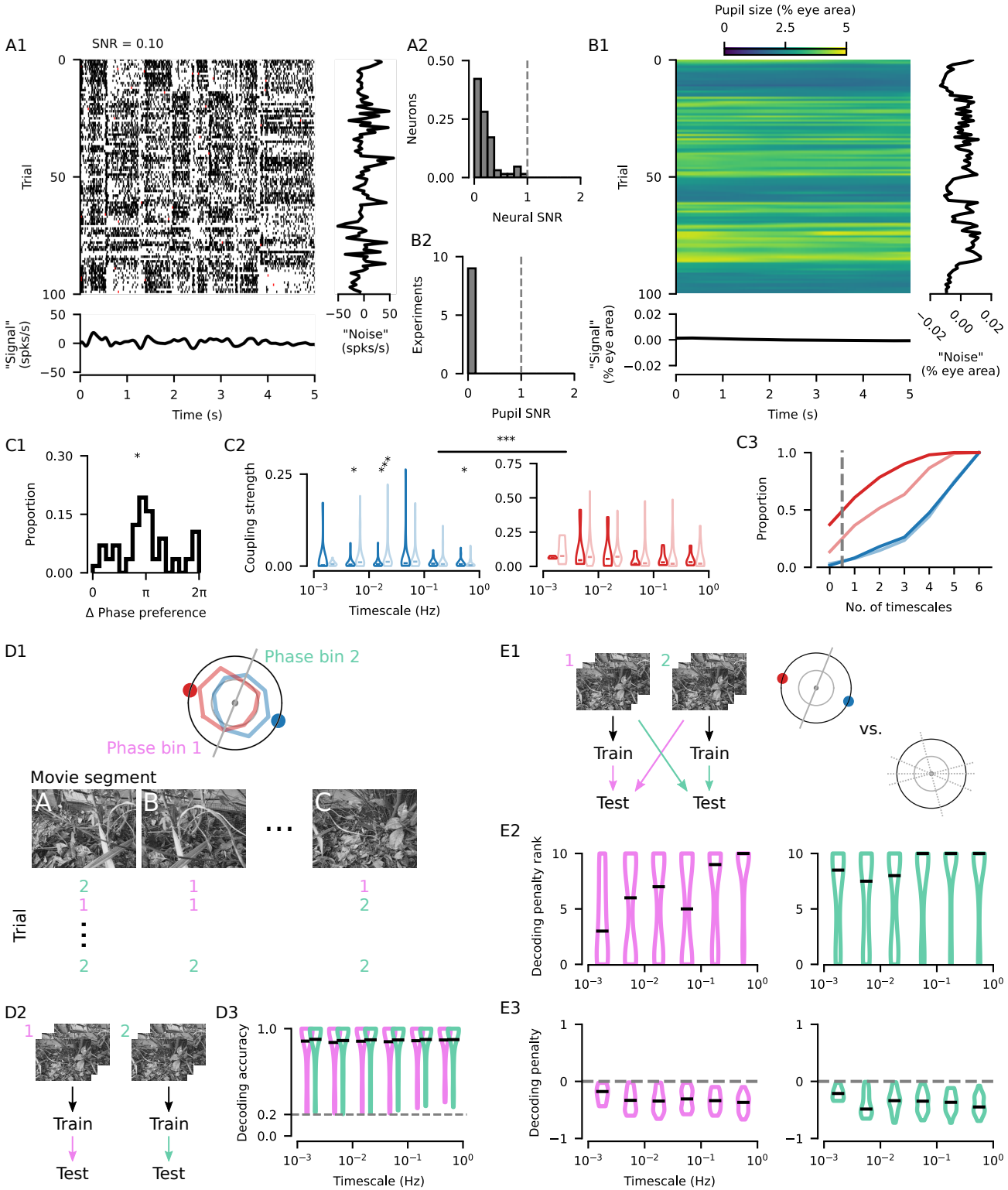
A1
SNR = 0.10
Trial
"Signal" (spks/s)
Time (s)
"Noise" (spks/s)
A2
Neurons
Neural SNR
B2
Experiments
Pupil SNR
B1
Pupil size (% eye area)
"Signal" (% eye area)
"Noise" (% eye area)
C1
Proportion
Δ Phase preference
C2
Coupling strength
Timescale (Hz)
C3
No. of timescales
D1
Phase bin 1
Phase bin 2
Movie segment
Trial
D2
Train
Test
D3
Decoding accuracy
E1
vs.
E2
Decoding penalty rank
E3
Decoding penalty

Figure 5 Coupling of dLGN activity to pupil dynamics is related to differences in visual stimulus encoding. (A1) Raster plot showing the responses of an example neuron to a movie (*black*: tonic spikes; *red*: burst spikes). *Bottom*: The mean response of the example neuron, centered on the mean across the response. *Right*: The mean firing rate on each trial, centered on the mean across trials. Note that the "Signal" and "Noise" axes have the same scale, illustrating that firing rate fluctuations across trials were larger than the fluctuations in firing rate that were induced by the stimulus. **(A2)** The signal-to-noise ratio (SNR) compares the variance in the mean stimulus response to the mean variance for matching time-points across trials (N = 64 neurons, see Methods). A SNR less than one indicates that the trial-to-trial changes in firing rate reflecting variability of internal state and overt behaviors are larger than the change induced by the stimulus. **(B1)** Same as (A1), for pupil size (same example experiment). **(B2)** The pupil SNR for all experiments is close to zero, indicating that stimulus induced fluctuations in pupil size were negligible compared to across-trial fluctuations. **(C1)** Difference in the preferred CPD coupling phase of bursts and tonic spikes, as in Figure 2D, but for neurons recorded during naturalistic stimulus viewing (V-test for non-uniform distribution with a mean of π: V = 16.2, p = 1.24×10^{-3}). **(C2)** Coupling strengths across temporal scales for all neuron-CPD pairs with significant coupling during stimulus viewing (*bold distributions*: coupling strengths during stimulus viewing, *faded distributions*: coupling strengths from Figure 2E, Mann-Whitney-U test for each timescale, p-value denoted by *asterisks*, * for $p\leq0.05$, ** for $p\leq0.01$, *** for $p\leq0.001$). As in Figure 2E, bursts were overall more strongly tuned than tonic spikes (*horizontal line, asterisks*: Wilcoxon rank-sum test for burst > tonic pooling across timescales). **(C3)** Cumulative distribution of the number of coupling timescales for each neuron. *Faded lines*: the distribution measured in the absence of a patterned visual stimulus (Figure 2F). *Bold lines*: the distribution measured during stimulus viewing. **(D1)** Schematic representation of how the data was partitioned in (D) and (E). Each trial of naturalistic stimulus presentation was split into five 1 s segments and a decoder was trained to identify the stimulus segment using spiking activity. Two decoders were trained for each neuron-CPD pair, one for each of two CPD phase groupings. *Turquoise*: Decoders trained on segments during which the CPD was in the phase bin where tonic spiking preferentially occurred. *Pink*: Decoders trained on segments during which the CPD was in the opposing phase bin, based on (C1) this is likely to be the phase preferred by bursting. **(D2)** Schematic of the movie segment decoding, initially performed by training and testing within data partitions. **(D3)** Decoding accuracy distributions for the two phase groupings for each CPD timescale. (*black lines*: median decoding accuracy). The *gray line* indicates chance-level performance. Decoding accuracy is generally high for both phase groupings. **(E1)** Schematic of the movie segment decoding, now performed by training a decoder on one of the data partitions and testing it on data from the other. The decoding performance across CPD phases was compared to the scores from (D3, within phases) to yield a "decoding penalty". This penalty was compared to the penalty obtained by repeating the same procedure on 10 random partitions of the data segments. A decoding penalty was considered significant if it was greater than the penalties obtained from all 10 random partitions. **(E2)** Distribution of the ranks of decoding penalties obtained from partitions based on CPD phases among those obtained from 10 random partitions (*black lines*: median rank). High ranks indicate that the penalty for training and testing across data partitions based on CPD phases were greater than those obtained by random partitions. **(E3)** Distributions of decoding penalties, only for neuron-CPD pairs with significant penalties (*Black lines*: median decoding penalty). The penalty for training and testing across CPD phases can be as high as 50% across most timescales, suggesting that all timescales of modulation contribute to substantial differences in how stimuli are encoded.

Discussion

Our results establish that activity in dLGN, the primary visual thalamic nucleus, is coupled to components of pupil dynamics that occur over multiple timescales, ranging from several seconds to several minutes. Throughout these timescales, bursts of spikes were more strongly coupled to the components of pupil dynamics than tonic spiking. Moreover, bursts and tonic spikes exhibited distinct phase preferences, with bursts and tonic spikes occurring during opposing phases across all timescales. The coupling between dLGN spiking and pupil dynamics could not be attributed to differences in pupil size *per se*, to transitions between quiescence and locomotion, or to eye movements. Furthermore, the coupling persisted even during viewing of a rich naturalistic movie, where we observed differences in how visual stimuli were encoded across phases of pupil dynamics. Together, our findings support the notion that arousal-related modulation of visual thalamus in the waking state involves a combination of changes in dLGN spiking activity linked to diverse temporal scales.

Our data-driven decomposition of the pupil signal moves beyond a binary classification of behavioral/arousal state and reveals components of pupil dynamics which can predict dLGN activity modulations across multiple timescales. It is important to note that the components we recovered here do not necessarily map directly onto the time-courses of independent internal processes or behavioral sequences. Yet, it is likely that the multi-scale modulations of both the pupil signal and dLGN neural activity results from a combination of multiple intrinsic and/or

extrinsic influences, possibly separated by their own temporal scale over which they occur. Multi-scale influences have been described in other contexts, including the presence of diverse activity timescales within and between neurons [38, 39], the action of several behavioral state-related neuromodulators with distinct timescales [25, 40] or the largely nonoverlapping activation dynamics of different ensembles of neurons within the same neuromodulatory system [41]. Furthermore, in freely moving paradigms, detailed quantification of behavior has revealed a nested organization, where rapid behaviors were shared in different sequential patterns of intermediate length as a function of the long-time animal's behavioral state [20]. Finally, during task performance, cognitive processes sensitive to neuromodulation can change on fast and slow timescales, such as quick reorienting to surprising stimuli or the choice of specific behavioral strategies over longer timescales [22].

Candidate sources for modulations of neural activity according to behavioral state in dLGN are the pupil-linked neuromodulators norepinepherine (NE) [21, 25, 42] and acetylcholine (ACh) [11, 25]. NE is provided to the thalamus by the locus coeruleus (LC) [43, 44], while ACh in the rodent thalamus comes from several brainstem nuclei (PPN/LDT and PBN) [45–47] and the basal forebrain (BF) [45, 48]. Consistent with a potential role for the LC-NE system in the present findings, stimulation of the LC *in vivo* has been shown to suppress bursting in the dLGN [49] and primary somatosensory thalamus (VPM) [50], while causing pupil dilation [42]. Although the activity of the cholinergic PPN/LDT and PBN has not been directly linked to pupil fluctuations, the effects of ACh on thalamic neurons are similar to those we observed during dilating phases of pupil dynamics: stimulation of the PPT/LDT increases firing rates in the VPM [51], and switches dLGN neurons from burst to tonic mode [52]. It is important to note that neuromodulatory influences in the thalamocortical system extend beyond direct effects on thalamic neurons, and also involve the thalamic reticular nucleus [45, 48, 53–55], corticothalamic L6 neurons [56, 57], and retinal boutons [58–60], all of which could contribute to additional arousal-related influences on thalamic neurons. Future studies directly tracking modulatory inputs into thalamus and decomposing their activity into distinct timescales promise to yield further insight into the relation between behavioral states and modulation of sensory processing.

The modulations in burst and tonic spiking we observed indicate that, throughout periods of wakefulness, and even during stimulus viewing, the dLGN is in constant alternation between two distinct information processing modes. One prominent view is that tonic spikes encode information about a stimulus linearly, while stimulus-driven bursts provide an all-or-none "wake-up call" to the cortex [14], by providing augmented retinogeniculate [37] and geniculocortical [18] communication, and improved stimulus detectability [61] (for related work in the somatosensory system, see e.g. [62, 63]). Burst spikes, in comparison with tonic spikes, also have different feature selectivity: they track low frequency stimulus content [9, 64, 65] with an earlier response phase [33, 36, 66], integrate input over longer time-scales with biphasic response kernels [35, 36, 67–69], and prefer smaller stimuli [70] with a stronger suppressive surround [36]. Such differences likely contribute to the decoding penalty we observed when training and testing decoders on spiking activity from opposing phases of the modulations we observed. However, it is

also possible that neuromodulatory mechanisms change the stimulus response properties of dLGN neurons, without eliciting a switch in firing mode from tonic spiking to bursting.

Our results focused on the commonalities of multi-scale modulation across the recorded population of dLGN neurons. However, we also observed a substantial diversity across neurons in the strength of coupling within a timescale, as well as diversity in the timescale with strongest coupling. The mouse dLGN consists of various cell types [71] and functional sub-types [72, 73], some of which are known to be differentially affected by arousal-linked variables [60, 74]. Moving forward, considering the specific functional role of a given neuron, along with its temporal structure of modulation, will lead to a better mechanistic understanding of dynamic stimulus processing in the visual system.

In this study, revealing the multi-scale, nested nature of arousal-related activity modulations in dLGN was possible by applying a decomposition approach to the pupil signal. This approach extends previous studies using raw pupil size as a marker for internal arousal processes in sensory circuits [7, 57, 59, 75–79] or the pupil's dynamics within a restricted frequency range [6, 25, 80]. Importantly, however, our analysis of pupil components and phases in relation to spiking activity does not undermine a role of pupil size itself, and, in fact, the two approaches can overlap in some cases. For example, coupling with a phase of 0 to a high-power component is likely to be reflected in a monotonic increasing relationship to pupil size. Hence, we view these approaches as complimentary, allowing us to gain a more nuanced and comprehensive perspective on the modulation of sensory processing.

While our study has expanded the use of the pupil signal to reveal arousal-related modulations to multiple temporal scales, recent work has emphasized that a larger array of behaviors may also help to better explain activity in sensory systems [19, 81]. Individual behaviors, such as running onset (Figure S3A, [see also 8, 12]), eye movements (Figure S4C, [see also 82]), head movements [83], or particular postures in freely moving conditions [84], modulate activity in the visual system. These modulations often occur in time-windows of seconds or less, which may be explained by the need to account for their immediate influence on sensory inputs [34, 85]. Our present work shows that sensory neurons are modulated not only at these faster timescales, but also to longer timescales ranging from tens to thousands of seconds. In the future, a more complete characterization of unrestricted, individual behaviors, and of their nested organization within sequences and states occurring on longer temporal scales [20], combined with measurements of neural responses, promises to advance our understanding of modulations of multi-scale sensory processing by behavioral state.

Materials and Methods

Resource Availability

Lead Contact

Requests for further information should be directed to the corresponding author, Laura Busse (busse@bio.lmu.de)

Data and Code Availability

The data and code required to generate the results and figures presented in this manuscript will be made publicly available upon publication.

Method Details

All procedures complied with the European Communities Council Directive 2010/63/EU and the German Law for Protection of Animals, and were approved by local authorities, following appropriate ethics review.

Surgical procedure

Experiments were carried out in 6 adult transgenic PV-Cre mice (median age at first recording session: 23.4 weeks; B6;129P2-Pvalb$^{tm1(cre)Arbr}$/J; Jackson Laboratory), 4 adult Ntsr1-Cre mice (median age: 24.7 weeks; B6.FVB(Cg)-Tg(Ntsr1-cre)GN220Gsat/Mmcd; MMRRC), and one wild-type BL6 mouse (age: 33.9 weeks), of either sex. Transgenic mice were used, as these mice were also included in another study [33] which required selective viral expression of ChR2 in area V1. For the present study, data mostly came from experiments where no optogenetic manipulation was present, with the exception of the data in Figure 5 and Figure S6.

The majority of experiments were performed under Licence ROB-55.2-2532.Vet_02-17-40. Thirty minutes prior to surgical procedures, mice were injected with an analgesic (Metamizole, 200 mg/kg, sc, MSD Animal Health, Brussels, Belgium). To induce anesthesia, animals were placed in an induction chamber and exposed to isoflurane (5% in oxygen, CP-Pharma, Burgdorf, Germany). After induction of anesthesia, mice were fixated in a stereotaxic frame (Drill & Microinjection Robot, Neurostar, Tuebingen, Germany). At the beginning of the surgical procedure, an additional analgesic was administered (Buprenorphine, 0.1 mg/kg, sc, Bayer, Leverkusen, Germany) and the isoflurane level was lowered (0.5%–2% in oxygen), such that a stable level of anesthesia could be achieved as judged by the absence of a pedal reflex. Throughout the procedure, the eyes were covered with an eye ointment (Bepanthen, Bayer, Leverkusen, Germany) and a closed loop temperature control system (ATC 1000, WPI Germany, Berlin, Germany) ensured that the animal's body temperature was maintained at 37°C. The animal's head was shaved and thoroughly disinfected using iodine solution (Braun, Melsungen, Germany). Before performing a scalp incision along the midline, a local analgesic was delivered (Lidocaine hydrochloride, sc, bela-pharm, Vechta, Germany). The

skin covering the skull was partially removed and cleaned from tissue residues with a drop of H_2O_2 (3%, AppliChem, Darmstadt, Germany). Using four reference points (bregma, lambda, and two points 2 mm to the left and to the right of the midline respectively), the animal's head was positioned into a skull-flat configuration. The exposed skull was covered with OptiBond FL primer and adhesive (Kerr dental, Rastatt, Germany) omitting three locations: V1 (AP: −2.8 mm, ML: −2.5 mm), dLGN (AP: −2.3 mm, ML: −2 mm), and a position roughly 1.5 mm anterior and 1 mm to the right of bregma, designated for a miniature reference screw (00-96 X 1/16 stainless steel screws, Bilaney) soldered to a custom-made connector pin. Unrelated to the purpose of this study, 2 μL of the adeno-associated viral vector rAAV9/1.EF1a.DIO.hChR2(H134R)-eYFP.WPRE.hGH (Addgene, #20298-AAV9) was dyed with 0.3 μL fast green (Sigma-Aldrich, St. Louis, USA), and after performing a small craniotomy over V1, a total of ∼0.5 μL of this mixture was injected across the entire depth of cortex (0.05 μL injected every 100 μm, starting at 1000 μm and ending at 100 μm below the brain surface), using a glass pipette mounted on a Hamilton syringe (SYR 10 μL 1701 RN no NDL, Hamilton, Bonaduz, Switzerland). A custom-made lightweight stainless steel head bar was positioned over the posterior part of the skull such that the round opening contained in the bar was centered on V1/dLGN and attached with dental cement (Ivoclar Vivadent, Ellwangen, Germany) to the primer/adhesive. The opening was later filled with the silicone elastomer sealant Kwik-Cast (WPI Germany, Berlin, Germany). At the end of the procedure, an antibiotic ointment (Imax, Merz Pharmaceuticals, Frankfurt, Germany) was applied to the edges of the wound and a long-term analgesic (Meloxicam, 2 mg/kg, sc, Böhringer Ingelheim, Ingelheim, Germany) was administered and continued to be administered for 3 consecutive days. For at least 5 days post-surgery, the animal's health status was assessed via a score sheet.

A smaller number of mice (N = 1) were treated in accordance with Licence CIN 4/12, in which general surgical procedures were identical to the foregoing with the following exceptions. After induction of anesthesia, mice were additionally injected with atropine (atropine sulfate, 0.3 mg/kg, s.c.; Braun). The head post consisted of a small S-shaped piece of aluminum, which was cemented to the skull between lambda and bregma and to the right of the midline. Posterior to the head post, overlying the cerebellum, two miniature screws serving as ground and reference were implanted. At the end of the procedure, antibiotics (Baytril, 5 mg/kg, s.c.; Bayer) and a long-term analgesic (Carprofen, 5 mg/kg, s.c.; Rimadyl, Zoetis) were administered and were given for 3 days after surgery.

After at least 1 week of recovery, animals were gradually habituated to the experimental setup by first handling them and then simulating the experimental procedure. To allow for virus expression, neural recordings started no sooner than 3 weeks after injection. On the day prior to the first day of recording, mice were fully anesthetized using the same procedures as described for the initial surgery, and a craniotomy (ca. 1.5 mm^2) was performed over dLGN and V1 and re-sealed with Kwik-Cast (WPI Germany, Berlin, Germany). As long as the animals did not show signs of discomfort, the long-term analgesic Metacam was administered only once at the end of surgery, to avoid any confounding effect on experimental results. Recordings were performed daily and continued for as long as the quality of the electrophysiological signals remained high.

Electrophysiological recordings

Mice were head-fixed on a styrofoam ball and allowed to run freely. Extracellular signals were recorded at 30 kHz (Blackrock Microsystems). For each recording session, the silicon plug sealing the craniotomy was removed. To record from dLGN, a 32 channel linear silicon probe (Neuronexus A1x32Edge-5mm-20-177-A32, Ann Arbor, USA) was lowered to a depth of ∼2700–3700 μm below the brain surface. We judged recording sites to be located in dLGN based on the characteristic progression of RFs from upper to lower visual field along the electrode shank [72] and the presence of responses strongly modulated at the temporal frequency of the drifting gratings (F1 response). For *post hoc* histological reconstruction of the recording site, the electrode was stained with DiI (Invitrogen, Carlsbad, USA) for one of the final recording sessions.

For the purposes of a different study [33], during recordings involving naturalistic movie stimulation (Figure 5, Figure S5, and trials, which were randomly interleaved with control trials. For the purposes of this study, only electrophysiological data from trials without optogenetic stimulation was considered.

Histology

After the final recording session under Licence ROB-55.2-2532.Vet_02-17-40, mice were first administered an analgesic (Metamizole, 200 mg/kg, sc, MSD Animal Health, Brussels, Belgium) and following a 30 min latency period were transcardially perfused under deep anesthesia using a cocktail of Medetomidin (Domitor, 0.5 mg/kg, Vetoquinol, Ismaning, Germany), Midazolam (Climasol, 5 mg/kg, Ratiopharm, Ulm, Germany) and Fentanyl (Fentadon, 0.05 mg/kg, Dechra Veterinary Products Deutschland, Aulendorf, Germany). A few animals, which were treated according to a different license, were anesthetized with sodium pentobarbital (Narcoren, 400 mg/kg, ip, Böhringer Ingelheim, Ingelheim, Germany). Perfusion was first done with Ringer's lactate solution followed by 4% paraformaldehyde (PFA) in 0.2 M sodium phosphate buffer (PBS).

To verify recording site and virus expression, we performed histological analyses. Brains were removed, postfixed in PFA for 24 h, and then rinsed with and stored in PBS at 4° C. Slices (40 μm) were cut using a vibrotome (Leica VT1200 S, Leica, Wetzlar, Germany), mounted on glass slides with Vectashield DAPI (Vector Laboratories, Burlingame, USA), and coverslipped. A fluorescent microscope (BX61, Olympus, Tokyo, Japan) was used to inspect slices for the presence of yellow fluorescent protein (eYFP) and DiI. Recorded images were processed using FIJI [86, 87].

For experiments under Licence CIN 4/12, general histological procedures were identical to those described above, except that mice were injected with sodium pentobarbital (Narcoren, = 200 mg/kg intraperitoneally; Böhringer Ingelheim) before perfusion. Coronal brain slices (50 μm) were obtained by using a vibratome (Microm HM 650V, Thermo Fisher Scientific) and inspected with a Zeiss Imager.Z1m fluorescent microscope (Zeiss).

Visual stimulation

Visual stimulation was presented using custom written software (EXPO, https://sites.google.com/a/nyu.edu/expo/home) on a liquid crystal display (LCD) monitor (Samsung SyncMaster 2233RZ, 47×29 cm, 1680×1050 resolution at 60 Hz, mean luminance 50 cd/m^2) positioned at a distance of 25 cm from the animal's right eye. The data presented in all figures, with the exception of Figure 5, Figure S5, and Figure S6, was recorded while animals were viewing either a static gray screen (N = 5 experiments) or a sparse noise stimulus (N = 10 experiments). The sparse noise stimulus consisted of non-overlapping white and black squares flashed for 200 ms on a square grid spanning 60 deg, while individual squares spanned 5 deg. The data presented in Figure 5 and Figure S6were recorded while the animals were repeatedly presented with 5 s naturalistic movie clips [as described in 33].

Behavioral tracking

During electrophysiological recording, head-fixed mice were allowed to run on an air cushioned Styrofoam ball. Ball movements were recorded by two optical computer mice which interfaced with a microcontroller (Arduino Duemilanove) and sampled ball movements at 90 Hz. Locomotor activity was quantified by computing the Euclidean norm of two perpendicular components of ball velocity (pitch and roll), and herein referred to as run speed or locomotion speed. Running bouts were defined as periods of time where the ball speed exceeded 1 cm/s for at least 2 s, with a break of no more than 2 s, and during which the run speed exceeded the threshold for at least half of the bout duration. Quiescence was defined as any period of time outside of a running bout.

In order to track pupil size, the stimulus-viewing eye was illuminated with and infrared LED light, and the eye was filmed with a camera (Guppy AVT camera; frame rate 50 Hz, Allied Vision, Exton, USA) equipped with a zoom lens (Navitar Zoom 6000). Pupil size was extracted from the videos using a custom, semi-automated algorithm. Each video frame was equalized using an adaptive bi-histogram equalization procedure, and then smoothed using median and bilateral filters. The center of the pupil was initially estimated by taking the darkest point in a convolution of the filtered image with a black square. Next, the peaks of the image gradient along lines extending radially from the center point were used to define the pupil contour. Lastly, an ellipse was fit to the contour, and the area of the ellipse was taken as pupil size, and the center of the ellipse was taken as the pupil position. Frames in which the eye was obscured, occurring during eye closure or grooming, were detected by applying a threshold to the mean pixel-wise difference between each frame and a reference frame compiled by taking the median of several manually selected frames during which the eye was open. Data points with eye closure, as well as the four points immediately adjacent, were excluded. Because the pupil size and eyelid closure are correlated, many periods when the pupil was at its smallest could not be analysed, including some periods of very low arousal and sleep-related states. Adjustable parameters in the above algorithm were set manually for each experiment. After ellipse fitting, data points at which the fitted pupil position, size, eccentricity, or rate of change, were outside of a plausible range were removed from consideration. Unreliable segments, occurring due to eye-closure, grooming, or unstable ellipse

fitting, were automatically removed according to *a priori* criteria. Cubic splines were used to interpolate over gaps of < 5 s, and the remaining segments of continuous data were smoothed with a Gaussian kernel ($\sigma = 250$ ms). From each recording session, we only included data from the single longest continuous segment of reliable pupil data (median = 1159 s, min = 596 s, max = 2507 s).

Pupil size signal decomposition

The pupil size signal was decomposed into intrinsic mode functions (IMFs, herein referred to as components of pupil dynamics, CPDs) by empirical mode decomposition (EMD) using the "EMD" Python package (https://emd.readthedocs.io/). In contrast to the original broad-band pupil size signal, the CPDs are locally narrow-band and thus amenable to Hilbert spectral analysis [88]. EMD extracts these components without pre-defines filters, and respects the non-stationary present in biological signals. To minimize edge effects during spectral analysis, each CPD was extrapolated from the beginning and end by mirroring the three closest peaks/troughs across the signal boundary, and interpolating between the mirrored extrema with 3rd-order Bernstein polynomials restricted by gradient at the signal edge. CPDs with fewer than 3 extrema were extended by mirroring the first derivatives. The Hilbert transform was applied to the extended CPDs using the SciPy signal library to obtain the complex-valued analytic signal of each CPD, from which the instantaneous phase and amplitude were respectively computed as the angle and length of the signal vector at each timepoint, and instantaneous frequency was given by the time derivative of the unwrapped phase. Only timepoints corresponding to the un-extrapolated signal were used in further analysis. Each CPD was assigned a characteristic timescale by taking the mean frequency across all time points weighted by the amplitudes. The relative power of each IMF was assigned by taking the power (squared amplitude) density of each CPD and expressing it as fraction of the sum of the power densities from all CPDs resulting from the decomposition. At this point, some of the lower frequency CPDs were eliminated from further consideration if they did not complete at least four cycles within the recording segment.

The relationships between CPDs were assessed using a permutation test designed to find periods of phase coupling between CPDs. The IMFs resulting from EMD, although broadly different in frequency content, are not guaranteed to be independent. Therefore the same aspect of pupil dynamics can end up being captured by multiple CPDs. To address this problem, we reasoned that if this mixing was occurring, it would reflected in transient periods of phase alignment between two CPDs. This alignment would appear as a peaks in the joint phase distribution of two CPDs, causing the distribution to deviate from uniformity. However, because the phase distribution of each CPD is not itself uniform, for each pair of simultaneously recorded CPDs we simulated the expected joint distribution given a lack of phase coupling by shuffling the cycle order of each CPD independently 1000 times. The real and simulated joint distributions were then compared to a uniform distribution using the Kullbach-Leibler divergence (Δ KLD, Figure S1D2). The CPDs were considered significantly coupled if the Δ KLD of the true joint distribution exceeded the 95th percentile of the Δ KLDs computed from the simulated distributions (p-value $<= 0.05$; Figure S1D1,

magenta outlines; Figure S1D2, right). The specific combination of phases driving the coupling was determined by asking which points in the joint phase space exceeded the 95th percentile of the simulated distributions at the same point (Figure S1D1, white outlines). These phase combinations were only considered significant if the Δ KLD indicated that the two CPDs were coupled. For the analysis in Figure S3B, the periods of time during which coupled CPDs passed through these phase combinations were excluded.

Spike sorting

For recordings under protocol ROB-55.2-2532.Vet_02-17-40, the spiking activity of isolated single units was initially extracted from extracellular recordings using the Kilosort spike-sorting toolbox [89]. The resulting spike clusters were subject to manual curation in Spyke [90], where spikes within a cluster were temporally aligned and plotted in a 3D space (multichannel PCA, ICA, and/or spike time). In this space, clusters could be merged to account for drift in spike shape over the recording session (for example, if the first two wave shape PCs changed smoothly as a function of spike time), or further split using a gradient-ascent based clustering algorithm [91]. Clusters containing only spikes with no consistent and clearly discernible voltage deflection were eliminated from further consideration. Finally, cluster auto-correlograms were examined to ensure that a clear refractory period was present; while the presence of a refractory period was not an indicator of a well-isolated unit, the absence of a refractory period was taken as an indicator that the cluster might need to be further split, or contained a high amount of noise. Remaining clusters were compared using empirical distance metrics to ensure that they were well separated.

For the few sessions recorded under protocol CIN 4/12, single neurons in our linear array recordings were isolated by grouping neighboring channels into five equally sized 'virtual octrodes' (8 channels per group with 2-channel overlap for 32 channel probes). Using an automatic spike detection threshold [92] multiplied by a factor of 1.5, spikes were extracted from the high-pass-filtered continuous signal for each group separately. The first three principal components of each channel were used for semi-automatic isolation of single neurons with KlustaKwik [93], and the resulting clusters were manually refined with Klusters [94]. Only clusters whose autocorrelogram displayed a clear refractory period and whose mean voltage trace showed a characteristic spike waveshape were further considered. To avoid duplication of neurons extracted from linear probe recordings, we computed cross-correlograms (1-ms bins) between pairs of neurons from neighboring groups. Pairs for which the cross-correlogram's zero bin was three times larger than the mean of non-zero-bins were considered to be in conflict, and only one was kept.

Bursts of action potentials are associated with a slow, hyperpolarization de-inactivated Ca^{2+} conductance present in thalamic neurons, which cannot be directly measured in extracellular recordings. However, studies combining intra- and extracellular recordings have established reliable empirical criteria for identification of these thalamic bursts [30], according to which $\geq$2 spikes with a prior period with no spiking of 100 ms and an ISI of $<$ 4 ms are part of a burst (Figure 2A). Spikes satisfying these criteria were categorized as burst spikes, whereas all other spikes were considered tonic spikes. Downstream analyses were performed separately on tonic spikes and burst events,

for which all spikes in a burst were treated as a single event. Among our recorded dLGN units, the vast majority (89.5%) displayed bursting events, which and accounted for 3% of dLGN spikes (burst ratio: the proportion of all spikes in the recording that were part of a burst; Figure S2A$_2$).

Short timescale serial dependence of burst events and tonic spiking was assessed by computing the auto-correlogram for each activity type in a -1 s to 1 s window. Taking the average auto-correlation over all neurons, it was determined by visual inspection that both event types had a primary peak lasting approximately 300 ms. Although we also note that the mean burst auto-correlation has a secondary peak, indicating rhythmicity in the $\sim$ 5 Hz range [13].

Modulation of spiking by pupil size

In order to assess the modulation of spiking activity by arousal states, we began by modeling pupil size as a function of pupil size. For each neurons, spike counts were collected in 250 ms bins, and sorted into 10 bins according to the min-max normalized pupil size. A neuron was considered to be significantly modulated by pupil size if a one-way ANOVA across the pupil size bins was significant, regardless of which pupil size bin had the highest firing rate.

In order to model how firing rates change as a function of pupil size, for each of the significantly modulate neurons (see above), we used a Poisson Generalized Additive Model (PoissonGAM) to predict spike counts in 250 ms bins as a function of pupil size. The assumption to this approach is that spike counts are generated by a modulated Poisson process, where the underlying rate is determined by an arousal-related variable such as pupil size. In contrast to Generalized Linear Models (GLMs), GAMs can capture diverse relationships between the predictor and response variable by modeling the relationship as a sum of multiple spline functions. Model specification and fitting were performed using PyGAM (https://pygam.readthedocs.io) package. The pupil size predictor was constructed using 20 splines, with a penalty on the second derivative to promote smoothness. A grid search over this smoothness regularizer was performed, and the model with the lowest generalized cross-validation score was retained (Figure 1C1). Fano factors (Figure 1C2 were computed by collecting spike count variances in 20 pupil size bins, and dividing these by the mean spike counts for each pupil size bin predicted by the PoissonGAM. We repeated the analysis in Figure 1C using the temporal derivative of the pupil size signal and found qualitatively similar results, while obtaining lower overall explained deviance (data not shown). Thus here we present only the results obtained using pupil size.

Phase coupling

In order to assess the modulation of spiking activity by arousal states, we developed a phase coupling analysis to relate events such as bursts and tonic spikes to the components of pupil dynamics (CPDs). We required that at least 8 bursts or tonic spikes occurred over the course of the recording segment for a neuron to be considered in this analysis. Considering tonic spikes and burst events from each neuron separately, the Hilbert phase of each

ongoing CPD was collected at times when bursts (the time of the first spike of the burst) and tonic spikes occurred. Although coupling might be directly assessed by compiling phase histograms and computing the circular mean of these phases, we adopted various bias-corrections resulting in a more stringent assessment of phase coupling.

Firstly, CPDs are not guaranteed to have a linear phase progression, which is beneficial in that they can capture naturalistic asymmetric wave shapes, but presents a difficulty when assessing phase coupling as the underlying distribution of phases could itself be biased. These biases could lead one to falsely infer phase coupling simply because more recording time may be spent in a certain phase, and therefore more spikes attributed to this phase. We therefore converted phases to circular ranks, yielding a uniform underlying distribution to which bursts and tonic spikes could be related [95]. The angle of the circular mean rank was then converted back to a phase using the original distribution, and this value was reported as the "preferred phase". Next, as the circular mean resultant vector length is a biased statistic (its value is inflated for small number of observations), we opted for an unbiased measure of phase coupling strength in order to allow comparison of coupling strength across units with different firing rates, between tonic spikes and bursts, and between conditions where spikes were sub-sampled from the recording period. Rather than using mean resultant vector length (R), we used its squared value, which can be easily bias-corrected [31]. We thus quantified coupling strength as

$$\hat{R}^2 = \frac{n}{n-1}(R^2 - \frac{1}{n}) \tag{1}$$

where R is the mean resultant vector length computed using the circular phase ranks, and n is the number of tonic spikes or bursts. Finally, we sought to assess the statistical significance of phase coupling with a measure that was insensitive to the short-term serial dependence of spike trains, which effectively reduces the degrees of freedom of the sample. We adopted the null hypothesis that, if there were no relationship between spiking activity and CPD phase, then the coupling strength of an CPD-neuron pair would be the same as that measured from a spike train with the same short-term structure, but with no relationship to the CPD. We tested coupling strengths against this null hypothesis by splitting burst and tonic spike trains into segments of 300 ms, which were shuffled in order to destroy the relationship between CPD phase and spiking activity, and then phase coupling to the IMF was assessed as described above. This procedure was repeated 1000 times for each CPD-neuron pair to compile a null-distribution coupling strengths. The true coupling strength was then compared to this distribution, and assigned an exact p-value (precise to 3 decimal places) based on how many elements of the null set had a higher coupling strength value.

In general, we computed phase coupling using all recorded spikes (Figure 2, Figure S3A). However, in order to account for the influence of spiking activity surrounding behaviors such as locomotion and eye movements (Figure 4, Figure S4, and Figure S5), we excluded spiking activity that occurred during these behaviors from consideration. To measure coupling during periods of quiescence, spike that occurred during running bouts were excluded, as well

as spike occurring 2 s before bout onset, and 4 s after bout offset. For coupling during running, spikes occurring during quiescence were excluded, as well as spikes occurring during the first and last 2 s of the bout, meaning that bouts shorter than 4 s in length were not considered. To eliminate the influence of peri-saccadic activity, we excluded spiking activity occurring in a time window from 1 s before to 2 s after the saccade.

Pupil size distribution matching

We observed that pupil size could co-vary with CPD phase (Figure 3A1), thus presenting a confound for genuine phase coupling. In order to control for effects of pupil size *per se* from the measurement of CPD phase coupling, we adopted a histogram matching procedure [96, 97] to minimize the differences in the distribution of pupil sizes across the phase bins of each CPD. For each CPD, the recording was split into segments based on four phase bins. For each visit to a phase bin, the mean pupil size during the visit was collected, and compiled into histogram (10 bins). From this histogram we assembled a "minimum common distribution" of pupil sizes across phase bins by selecting the phase bin with the smallest number of entries in each pupil size bin. For each of these entries, we collected the entry from the other three phase bins with the closest pupil size, thus obtaining a number of samples matching the minimum common distribution from each phase bin. To assess the efficacy of this procedure, we computed the pair-wise difference in mean pupil size distribution (this time taking into account the full range of pupil sizes from each bin visit, rather than the mean) between each pair of phase bins, and took the maximum difference. We then compared this difference before and after sub-sampling to match for pupil size (Figure 3A1). The phase coupling analysis presented in Figure 3 results from taking only spikes that occurred during the sub-sampled time periods from the matching procedure.

Correlation analyses

Locomotion speed is known to be reflected in the pupil size signal (Figure S1B3, [8]). In order to assess the potential contributions of locomotion speed to the phase coupling we observed, we performed correlation analyses relating each CPD to the animal's locomotion speed. Because serial dependence in signals can inflate correlation values and violates the independence assumption required to directly calculate a p-value, we adopted a permutation-based approach to assess the statistical significance of CPD-speed cross-correlations [98]. Each CPD was correlated with 1000 run speed traces collected from other experiments, and compared the peak value cross-correlation to the distribution of nonsense correlations in order to obtain a p-value. To further reduce the detection of spurious correlations, we limited our search for the peak to lags in the range of [-T, T], where T is the mean period of the CPD. For example, for a CPD with a mean period of 5 s, the search window would be restricted to lags of [-10 s, 10 s], and maximum value of the absolute cross-correlation in this window would be compared to the distribution of nonsense correlations. The cross-correlation was considered significant only if the maximum value within the prescribed range had a p-value ≤ 0.05.

Spiking responses

To compute spiking responses to behavioral events (running onsets, running offsets, saccades) and experimental events (stimulus onsets), we first estimated the instantaneous firing rate surrounding each event via kernel density estimation ([99], implemented in the `statistics.instantaneous_rate` function from https://elephant.readthedocs.io). Instantaneous rates were estimated using a Gaussian kernel 100 ms bandwidth and sampled with a resolution of 50 ms. In the case of sacccade responses (Figure S5C), K-means clustering (`sklearn.clustering.KMeans`, with k=3) was performed after taking the top principal components (explaining 80% of the variance) of the mean responses of each neuron in a window of [-1s, 1s] surrounding the saccade. To quantify the trial-to-trial variability in stimulus responses (Figure 5A2 and Figure 5B2), we constructed a signal to noise ratio comparing the variance across time of the mean stimulus response to the mean across-trial variance for each time point.

$$\mathrm{SNR} = \frac{\mathrm{Var}_l(\mathrm{E}_k(X))}{\mathrm{E}_l(\mathrm{Var}_k(X))} \tag{2}$$

Where $X = [x_1, ..., x_k]^T \in R^{K,L}$ is the response matrix compiled from K trials of duration L, and $\mathrm{E}_d()$ and $\mathrm{Var}_d()$ denote taking the mean or variance across the indicated dimension of the matrix.

Decoding analyses

For each CPD-neuron combination, we trained support-vector classifiers (SVCs) using the Scikit-Learn Python library (`sklearn.svm.SVC`) to decode CPD phase and visual stimuli from spiking activity during naturalistic stimulus viewing (Figure 5, Figure S6). Spike times (tonic spike times, burst times, or all spikes) from each trial were converted into instantaneous rates (see above), and each 5 s trial was split into 1 s segments. To decode CPD phase (Figure S6), we assigned a label to each 1 s segment of activity by taking the circular mean phase of the CPD during the segment, and placing this mean phase into one of two phase bins. We then trained an SVC (with a radial basis function kernel) to decode the phase label using only burst rates or only tonic spike rates occurring during the 1 s segment, and assessed the decoding performance with5-fold cross-validation. To decode the visual stimulus (Figure 5D), we assigned each 1 s segment with a label (e.g. 1 for the first second of the stimulus, 5 for the last second of the stimulus), and then split the segments into two groups according to the mean CPD phase during the segment. We used the instantaneous rates (estimates using all spikes together regardless of their categorization as tonic or burst) from one group to train an SVC (with a linear kernel) to performed "one-versus-rest" decoding of the stimulus labels, and tested the decoder using the same data as well as the data from the other group. We took the difference in decoding scores between the two groups as the "decoding penalty". We compared the decoding penalty obtained when splitting the segments by CPD phase to the decoding penalties obtained from 10 random splits of the data as a control. The decoding penalty for the CPD-neuron pair was considered significant if it was greater than all 10 random splits. In both of the above decoding schemes, we determined the two CPD phase bins based on the

preferred coupling of each neuron: one bin was centered around the preferred phase of tonic spiking of the neuron (preferred phase $\pm\ \pi/2$), and the other bin was centered around the opposing phase (preferred phase - $\pi \pm \pi/2$).

Acknowledgements

This research was supported by the German Research Foundation (DFG) RTG2175 "Perception in context and its neural basis" (CL), DFG SFB 870 "Assembly and function of neural circuits", TP 19 (118803580) (LB), DFG SFB 1233 "Robust Vision: Inference Principles and Neural Mechanisms", TP 13 (276693517) and by the SmartStart program of the Bernstein Network for Computational Neuroscience funded by the Volkswagen Foundation (DC). We would like to thank M. Sotgia for lab management and support with animal handling and histology, Y. Bauer, G. Born, and A. Kotkat for their contributions to the data collections and spike sorting, S. Schörnich for IT support, and B. Grothe for providing excellent research infrastructure.

Author Contributions

Davide Crombie: Conceptualization, Methodology, Software, Formal analysis, Data Curation, Writing, Writing - Review & Editing, Visualization, Funding acquisition. **Martin A. Spacek**: Software, Investigation, Data Curation. **Laura Busse**: Conceptualization, Methodology, Writing, Writing - Review & Editing, Project Administration, Supervision, Funding Acquisition. **Christian Leibold**: Conceptualization, Methodology, Writing, Writing - Review & Editing, Project Administration, Supervision, Funding Acquisition.

Declaration of Interests

The authors declare no competing interests.

References

[1] Harris KD, Thiele A. Cortical state and attention. Nature Reviews Neuroscience. 2011;12(9):509–523.

[2] McGinley MJ, Vinck M, Reimer J, Batista-Brito R, Zagha E, Cadwell CR, et al. Waking state: rapid variations modulate neural and behavioral responses. Neuron. 2015;87(6):1143–1161.

[3] McCormick DA, Nestvogel DB, He BJ. Neuromodulation of brain state and behavior. Annual review of neuroscience. 2020;43:391–415.

[4] Poulet JF, Crochet S. The cortical states of wakefulness. Frontiers in Systems Neuroscience. 2019;12:64.

[5] Hess EH, Polt JM. Pupil size as related to interest value of visual stimuli. Science. 1960;132(3423):349–350.

[6] Reimer J, Froudarakis E, Cadwell CR, Yatsenko D, Denfield GH, Tolias AS. Pupil fluctuations track fast switching of cortical states during quiet wakefulness. Neuron. 2014;84(2):355–362.

[7] McGinley MJ, David SV, McCormick DA. Cortical membrane potential signature of optimal states for sensory signal detection. Neuron. 2015;87(1):179–192.

[8] Vinck M, Batista-Brito R, Knoblich U, Cardin JA. Arousal and locomotion make distinct contributions to cortical activity patterns and visual encoding. Neuron. 2015;86(3):740–754.

[9] Bezdudnaya T, Cano M, Bereshpolova Y, Stoelzel CR, Alonso JM, Swadlow HA. Thalamic burst mode and inattention in the awake LGNd. Neuron. 2006;49(3):421–432.

[10] Steriade M, McCormick DA, Sejnowski TJ. Thalamocortical oscillations in the sleeping and aroused brain. Science. 1993;262(5134):679–685.

[11] McCormick DA. Neurotransmitter actions in the thalamus and cerebral cortex and their role in neuromodulation of thalamocortical activity. Progress in Neurobiology. 1992;39(4):337–388.

[12] Erisken S, Vaiceliunaite A, Jurjut O, Fiorini M, Katzner S, Busse L. Effects of Locomotion Extend throughout the Mouse Early Visual System. Current Biology. 2014;24(24):2899–2907. doi:10.1016/j.cub.2014.10.045.

[13] Nestvogel DB, McCormick DA. Visual Thalamocortical Mechanisms of Waking State Dependent Activity and Alpha Oscillations. Neuron. 2022;1(5):120–138.e4. doi:https://doi.org/10.1016/j.neuron.2021.10.005.

[14] Sherman SM. Tonic and burst firing: dual modes of thalamocortical relay. Trends in Neurosciences. 2001;24(2):122–126.

[15] Alonso JM, Usrey WM, Reid RC. Precisely Correlated Firing in Cells of the Lateral Geniculate Nucleus. Nature. 1996;383(6603):815–819. doi:10.1038/383815a0.

[16] Kremkow J, Perrinet LU, Masson GS, Aertsen A. Functional Consequences of Correlated Excitatory and Inhibitory Conductances in Cortical Networks. Journal of Computational Neuroscience. 2010;28(3):579–594. doi:10.1007/s10827-010-0240-9.

[17] Bruno RM. Synchrony in Sensation. Current Opinion in Neurobiology. 2011;21(5):701–708. doi:10.1016/j.conb.2011.06.003.

[18] Swadlow HA, Gusev AG. The impact of'bursting'thalamic impulses at a neocortical synapse. Nature Neuroscience. 2001;4(4):402–408.

[19] Stringer C, Pachitariu M, Steinmetz N, Reddy CB, Carandini M, Harris KD. Spontaneous behaviors drive multidimensional, brainwide activity. Science. 2019;364(6437):255–255.

[20] Marshall JD, Aldarondo DE, Dunn TW, Wang WL, Berman GJ, Ölveczky BP. Continuous whole-body 3D kinematic recordings across the rodent behavioral repertoire. Neuron. 2021;109(3):420–437.

[21] Aston-Jones G, Cohen JD. An integrative theory of locus coeruleus-norepinephrine function: adaptive gain and optimal performance. Annu Rev Neurosci. 2005;28:403–450.

[22] Totah NK, Logothetis NK, Eschenko O. Noradrenergic ensemble-based modulation of cognition over multiple timescales. Brain Research. 2019;1709:50–66.

[23] Cohen JY, Amoroso MW, Uchida N. Serotonergic neurons signal reward and punishment on multiple timescales. Elife. 2015;4:e06346.

[24] Parikh V, Kozak R, Martinez V, Sarter M. Prefrontal acetylcholine release controls cue detection on multiple timescales. Neuron. 2007;56(1):141–154.

[25] Reimer J, McGinley MJ, Liu Y, Rodenkirch C, Wang Q, McCormick DA, et al. Pupil fluctuations track rapid changes in adrenergic and cholinergic activity in cortex. Nature Communications. 2016;7(1):1–7.

[26] Williamson RS, Hancock KE, Shinn-Cunningham BG, Polley DB. Locomotion and task demands differentially modulate thalamic audiovisual processing during active search. Current Biology. 2015;25(14):1885–1891.

[27] Hess EH, Polt JM. Pupil size in relation to mental activity during simple problem-solving. Science. 1964;143(3611):1190–1192.

[28] Schriver BJ, Bagdasarov S, Wang Q. Pupil-linked arousal modulates behavior in rats performing a whisker deflection direction discrimination task. Journal of Neurophysiology. 2018;120(4):1655–1670.

[29] de Gee JW, Tsetsos K, Schwabe L, Urai AE, McCormick D, McGinley MJ, et al. Pupil-linked phasic arousal predicts a reduction of choice bias across species and decision domains. Elife. 2020;9:e54014.

[30] Lu SM, Guido W, Sherman SM. Effects of membrane voltage on receptive field properties of lateral geniculate neurons in the cat: contributions of the low-threshold Ca2+ conductance. Journal of Neurophysiology. 1992;68(6):2185–2198.

[31] Kutil R. Biased and unbiased estimation of the circular mean resultant length and its variance. Statistics. 2012;46(4):549–561.

[32] Niell CM, Stryker MP. Modulation of visual responses by behavioral state in mouse visual cortex. Neuron. 2010;65(4):472–479.

[33] Spacek MA, Crombie D, Bauer Y, Born G, Liu X, Katzner S, et al. Robust effects of corticothalamic feedback and behavioral state on movie responses in mouse dLGN. Elife. 2022;11:e70469.

[34] Wurtz RH. Neuronal mechanisms of visual stability. Vision research. 2008;48(20):2070–2089.

[35] Lesica NA, Stanley GB. Encoding of natural scene movies by tonic and burst spikes in the lateral geniculate nucleus. Journal of Neuroscience. 2004;24(47):10731–10740.

[36] Alitto HJ, Weyand TG, Usrey WM. Distinct properties of stimulus-evoked bursts in the lateral geniculate nucleus. Journal of Neuroscience. 2005;25(2):514–523.

[37] Alitto H, Rathbun DL, Vandeleest JJ, Alexander PC, Usrey WM. The augmentation of retinogeniculate communication during thalamic burst mode. Journal of Neuroscience. 2019;39(29):5697–5710.

[38] Zeraati R, Shi YL, Steinmetz NA, Gieselmann MA, Thiele A, Moore T, et al. Intrinsic timescales in the visual cortex change with selective attention and reflect spatial connectivity. Nature communications. 2023;14(1):1858.

[39] Cavanagh SE, Hunt LT, Kennerley SW. A diversity of intrinsic timescales underlie neural computations. Frontiers in Neural Circuits. 2020;14:615626.

[40] Collins L, Francis J, Emanuel B, McCormick DA. Cholinergic and noradrenergic axonal activity contains a behavioral-state signal that is coordinated across the dorsal cortex. Elife. 2023;12:e81826.

[41] Noei S, Zouridis IS, Logothetis NK, Panzeri S, Totah NK. Distinct ensembles in the noradrenergic locus coeruleus are associated with diverse cortical states. Proceedings of the National Academy of Sciences. 2022;119(18):e2116507119. doi:10.1073/pnas.2116507119.

[42] Joshi S, Li Y, Kalwani RM, Gold JI. Relationships between pupil diameter and neuronal activity in the locus coeruleus, colliculi, and cingulate cortex. Neuron. 2016;89(1):221–234.

[43] Lindvall O, Björklund A, Nobin A, Stenevi U. The adrenergic innervation of the rat thalamus as revealed by the glyoxylic acid fluorescence method. Journal of Comparative Neurology. 1974;154(3):317–347.

[44] Mackay-Sim A, Sefton AJ, Martin PR. Subcortical projections to lateral geniculate and thalamic reticular nuclei in the hooded rat. Journal of Comparative Neurology. 1983;213(1):24–35.

[45] Hallanger AE, Levey AI, Lee HJ, Rye DB, Wainer BH. The origins of cholinergic and other subcortical afferents to the thalamus in the rat. Journal of Comparative Neurology. 1987;262(1):105–124.

[46] Sokhadze G, Seabrook TA, Guido W. The absence of retinal input disrupts the development of cholinergic brainstem projections in the mouse dorsal lateral geniculate nucleus. Neural Development. 2018;13(1):1–15.

[47] Huerta-Ocampo I, Hacioglu-Bay H, Dautan D, Mena-Segovia J. Distribution of Midbrain Cholinergic Axons in the Thalamus. eneuro. 2019;7(1):ENEURO.0454–19.2019. doi:10.1523/eneuro.0454-19.2019.

[48] Sokhadze G, Campbell PW, Guido W. Postnatal development of cholinergic input to the thalamic reticular nucleus of the mouse. European Journal of Neuroscience. 2019;49(8):978–989.

[49] Holdefer RN, Jacobs BL. Phasic Stimulation of the Locus Coeruleus: Effects on Activity in the Lateral Geniculate Nucleus. Experimental Brain Research. 1994;100(3):444–452. doi:10.1007/BF02738404.

[50] Rodenkirch C, Liu Y, Schriver BJ, Wang Q. Locus coeruleus activation enhances thalamic feature selectivity via norepinephrine regulation of intrathalamic circuit dynamics. Nature Neuroscience. 2019;22(1):120–133.

[51] Castro-Alamancos MA, Oldford E. Cortical sensory suppression during arousal is due to the activity-dependent depression of thalamocortical synapses. The Journal of Physiology. 2002;541(1):319–331.

[52] Lu SM, Guido W, Sherman SM. The brain-stem parabrachial region controls mode of response to visual stimulation of neurons in the cat's lateral geniculate nucleus. Visual Neuroscience. 1993;10(4):631–642.

[53] Asanuma C. Noradrenergic innervation of the thalamic reticular nucleus: a light and electron microscopic immunohistochemical study in rats. Journal of Comparative Neurology. 1992;319(2):299–311.

[54] Bickford M, Günlük A, Van Horn S, Sherman S. GABAergic projection from the basal forebrain to the visual sector of the thalamic reticular nucleus in the cat. Journal of Comparative Neurology. 1994;348(4):481–510.

[55] Woolf NJ, Butcher LL. Cholinergic systems in the rat brain: III. Projections from the pontomesencephalic tegmentum to the thalamus, tectum, basal ganglia, and basal forebrain. Brain Research bulletin. 1986;16(5):603–637.

[56] Sundberg SC, Lindström SH, Sanchez GM, Granseth B. Cre-expressing neurons in visual cortex of Ntsr1-Cre GN220 mice are corticothalamic and are depolarized by acetylcholine. Journal of Comparative Neurology. 2018;526(1):120–132.

[57] Augustinaite S, Kuhn B. Complementary Ca2+ Activity of Sensory Activated and Suppressed Layer 6 Corticothalamic Neurons Reflects Behavioral State. Current Biology. 2020;30(20):3945–3960. doi:10.1016/j.cub.2020.07.069.

[58] Chen C, Regehr WG. Presynaptic modulation of the retinogeniculate synapse. Journal of Neuroscience. 2003;23(8):3130–3135.

[59] Liang L, Fratzl A, Reggiani JDS, El Mansour O, Chen C, Andermann ML. Retinal Inputs to the Thalamus Are Selectively Gated by Arousal. Current Biology. 2020;30(20):3923–3934. doi:10.1016/j.cub.2020.07.065.

[60] Reggiani JDS, Jiang Q, Barbini M, Lutas A, Liang L, Fernando J, et al. Brainstem serotonin neurons selectively gate retinal information flow to thalamus. Neuron. 2023;111(5):711–726.e11. doi:10.1016/j.neuron.2022.12.006.

[61] Guido W, Weyand T. Burst responses in thalamic relay cells of the awake behaving cat. Journal of Neurophysiology. 1995;74(4):1782–1786.

[62] Borden PY, Wright NC, Morrissette AE, Jaeger D, Haider B, Stanley GB. Thalamic bursting and the role of timing and synchrony in thalamocortical signaling in the awake mouse. Neuron. 2022;110(17):2836–2853.e8. doi:10.1016/j.neuron.2022.06.008.

[63] Whitmire CJ, Waiblinger C, Schwarz C, Stanley GB. Information Coding through Adaptive Gating of Synchronized Thalamic Bursting. Cell Reports. 2016;14(4):795–807. doi:10.1016/j.celrep.2015.12.068.

[64] Mukherjee P, Kaplan E. Dynamics of neurons in the cat lateral geniculate nucleus: in vivo electrophysiology and computational modeling. Journal of Neurophysiology. 1995;74(3):1222–1243.

[65] Reinagel P, Godwin D, Sherman SM, Koch C. Encoding of visual information by LGN bursts. Journal of Neurophysiology. 1999;81(5):2558–2569.

[66] Grubb MS, Thompson ID. Visual response properties of burst and tonic firing in the mouse dorsal lateral geniculate nucleus. Journal of Neurophysiology. 2005;93(6):3224–3247.

[67] Lesica NA, Weng C, Jin J, Yeh CI, Alonso JM, Stanley GB. Dynamic encoding of natural luminance sequences by LGN bursts. PLoS Biol. 2006;4(7):e209.

[68] Mease RA, Kuner T, Fairhall AL, Groh A. Multiplexed spike coding and adaptation in the thalamus. Cell Reports. 2017;19(6):1130–1140.

[69] Zeldenrust F, Chameau P, Wadman WJ. Spike and burst coding in thalamocortical relay cells. PLOS Computational Biology. 2018;14(2):1–36. doi:10.1371/journal.pcbi.1005960.

[70] Rivadulla C, Martinez L, Grieve KL, Cudeiro J. Receptive field structure of burst and tonic firing in feline lateral geniculate nucleus. The Journal of Physiology. 2003;553(2):601–610.

[71] Kerschensteiner D, Guido W. Organization of the dorsal lateral geniculate nucleus in the mouse. Visual Neuroscience. 2017;34.

[72] Piscopo DM, El-Danaf RN, Huberman AD, Niell CM. Diverse visual features encoded in mouse lateral geniculate nucleus. Journal of Neuroscience. 2013;33(11):4642–4656.

[73] Rosón MR, Bauer Y, Kotkat AH, Berens P, Euler T, Busse L. Mouse dLGN receives functional input from a diverse population of retinal ganglion cells with limited convergence. Neuron. 2019;102(2):462–476.

[74] Aydın Ç, Couto J, Giugliano M, Farrow K, Bonin V. Locomotion modulates specific functional cell types in the mouse visual thalamus. Nature Communications. 2018;9(1):1–12.

[75] Molnár B, Sere P, Bordé S, Koós K, Zsigri N, Horváth P, et al. Cell-Type Specific Arousal-Dependent Modulation of Thalamic Activity in the Lateral Geniculate Nucleus. Cerebral Cortex Communications. 2021;doi:10.1093/texcom/tgab020.

[76] Neske GT, Nestvogel D, Steffan PJ, McCormick DA. Distinct waking states for strong evoked responses in primary visual cortex and optimal visual detection performance. Journal of Neuroscience. 2019;39(50):10044–10059.

[77] Petty GH, Kinnischtzke AK, Hong YK, Bruno RM. Effects of arousal and movement on secondary somatosensory and visual thalamus. eLife. 2021;10. doi:10.7554/elife.67611.

[78] Schröder S, Steinmetz NA, Krumin M, Pachitariu M, Rizzi M, Lagnado L, et al. Arousal Modulates Retinal Output. Neuron. 2020;107(3):487–495.e9. doi:10.1016/j.neuron.2020.04.026.

[79] Schwartz ZP, Buran BN, David SV. Pupil-associated states modulate excitability but not stimulus selectivity in primary auditory cortex. Journal of Neurophysiology. 2020;123(1):191–208.

[80] Okun M, Steinmetz NA, Lak A, Dervinis M, Harris KD. Distinct structure of cortical population activity on fast and infraslow timescales. Cerebral Cortex. 2019;29(5):2196–2210.

[81] Parker PRL, Brown MA, Smear MC, Niell CM. Movement-Related Signals in Sensory Areas: Roles in Natural Behavior. Trends in Neurosciences. 2020;doi:10.1016/j.tins.2020.05.005.

[82] Parker PR, Martins DM, Leonard ES, Casey NM, Sharp SL, Abe ET, et al. A dynamic sequence of visual processing initiated by gaze shifts. BioRxiv. 2022; p. 2022–08.

[83] Bouvier G, Senzai Y, Scanziani M. Head movements control the activity of primary visual cortex in a luminance-dependent manner. Neuron. 2020;108(3):500–511.

[84] Orlowska-Feuer P, Ebrahimi AS, Zippo AG, Petersen RS, Lucas RJ, Storchi R. Look-up and look-down neurons in the mouse visual thalamus during freely moving exploration. Current Biology. 2022;32(18):3987–3999.

[85] Saleem AB, Busse L. Interactions between rodent visual and spatial systems during navigation. Nature Reviews Neuroscience. 2023;doi:10.1038/s41583-023-00716-7.

[86] Rueden CT, Schindelin J, Hiner MC, DeZonia BE, Walter AE, Arena ET, et al. ImageJ2: ImageJ for the next Generation of Scientific Image Data. BMC Bioinf. 2017;18(1). doi:10.1186/s12859-017-1934-z.

[87] Schindelin J, Arganda-Carreras I, Frise E, Kaynig V, Longair M, Pietzsch T, et al. Fiji: An Open-Source Platform for Biological-Image Analysis. Nat Methods. 2012;9(7):676–682. doi:10.1038/nmeth.2019.

[88] Huang NE, Shen Z, Long SR, Wu MC, Shih HH, Zheng Q, et al. The empirical mode decomposition and the Hilbert spectrum for nonlinear and non-stationary time series analysis. Proceedings of the Royal Society of London Series A: mathematical, physical and engineering sciences. 1998;454(1971):903–995.

[89] Pachitariu M, Steinmetz NA, Kadir SN, Carandini M, Harris KD. Fast and Accurate Spike Sorting of High-Channel Count Probes with KiloSort. In: Lee DD, Sugiyama M, Luxburg UV, Guyon I, Garnett R, editors. Advances in Neural Information Processing Systems 29. Curran Associates, Inc.; 2016. p. 4448–4456.

[90] Spacek MA, Blanche TJ, Swindale NV. Python for large-scale electrophysiology. Front Neuroinform. 2009;2:9. doi:10.3389/neuro.11.009.2008.

[91] Swindale NV, Spacek MA. Spike sorting for polytrodes: a divide and conquer approach. Front Syst Neurosci. 2014;8:6. doi:10.3389/fnsys.2014.00006.

[92] Quiroga RQ, Nadasdy Z, Ben-Shaul Y. Unsupervised spike detection and sorting with wavelets and superparamagnetic clustering. Neural Comput. 2004;16(8):1661–87. doi:10.1162/089976604774201631.

[93] Henze DA, Borhegyi Z, Csicsvari J, Mamiya A, Harris KD, Buzsaki G. Intracellular Features Predicted by Extracellular Recordings in the Hippocampus In Vivo. Journal of Neurophysiology. 2000;84(1):390–400.

[94] Hazan L, Zugaro M, Buzsaki G. Klusters, NeuroScope, NDManager: A free software suite for neurophysiological data processing and visualization. Journal of Neuroscience Methods. 2006;155(2):207–216.

[95] Siapas AG, Lubenov EV, Wilson MA. Prefrontal phase locking to hippocampal theta oscillations. Neuron. 2005;46(1):141–151.

[96] Churchland MM, Byron MY, Cunningham JP, Sugrue LP, Cohen MR, Corrado GS, et al. Stimulus onset quenches neural variability: a widespread cortical phenomenon. Nature Neuroscience. 2010;13(3):369–378.

[97] Stuart EA. Matching methods for causal inference: A review and a look forward. Statistical science: a review journal of the Institute of Mathematical Statistics. 2010;25(1):1.

[98] Harris KD. Nonsense correlations in neuroscience. bioRxiv. 2020;.

[99] Shimazaki H, Shinomoto S. Kernel bandwidth optimization in spike rate estimation. Journal of computational neuroscience. 2010;29:171–182.

Supplemental Information

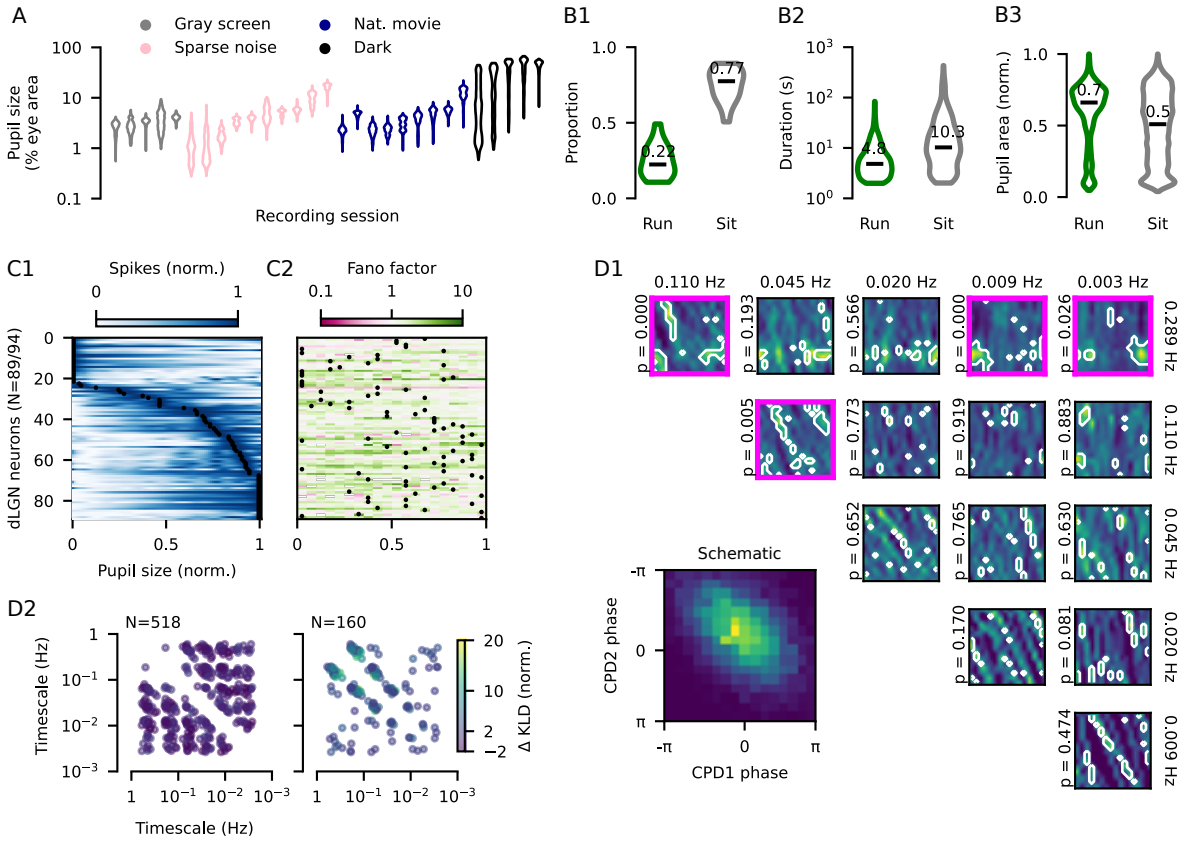

Figure S1 **(A)** Pupil size distributions for all recording sessions. Pupil size is expressed as a fraction of the total exposed eye area. Data from the spontaneous and sparse noise sessions are grouped together for the analyses in Figure 1, Figure 2, Figure S2, Figure S3B, Figure S3C, Figure 4, and Figure S4. **(B1)** Distribution of proportion of time spent in a running bout (*green*, see Methods) versus sitting (*grey*). *Horizontal bars* indicate the median proportions. **(B2)** Distribution of running bout and inter-bout-interval lengths. **(B3)** Distribution of pupil sizes (min-max normalized) during running and sitting. **(C1)** Modeled spike counts (min-max normalized) across pupil sizes for neurons from recordings performed in darkness with significant modulation (94.7%, ANOVA $p \leq 0.05$) neurons. The majority of modulated neurons (65.2%) had their maximum firing rates outside of the 90th percentile of pupil size. Neurons are sorted by the location of the maximum firing rate (*black dots*). **(C2)** Fano factor (spike count variance / predicted mean) across pupil size bins for the neurons in (C1). The mean Fano factor (spike count variance / mean predicted spike count) across pupil size bins and neurons was significantly greater than 1 (Wilcoxon rank-sum test: $W = 123.0$, $p = 1.5\times10^{-14}$). *Black dots*: Pupil size with the highest spike count variance for each neuron. **(D1)** Joint phase distribution for the CPDs from the recording in Figure 1B, illustrating the results of our statistical test for phase coupling between CPDs (see Methods). *Magenta outlines* indicate CPD pairs where the distribution as a whole showed that the CPDs were coupled ($p \leq 0.05$). *White outlines* illustrate the specific regions in the joint phase space where coupling might have occurred. **(D2)** Phase coupling z-scores quantifying the amount of coupling thought to be occurring between two simultaneously recorded CPDs (see Methods). *Left*: CPD pairs without significant coupling (76.4%). *Right*: CPD pairs with significant phase coupling (23.6%). The majority of CPDs did not have any coupling, suggesting that they represent independent aspects of pupil dynamics. Those that had coupling tended to be similar in temporal scale (i.e. were close to the diagonal).

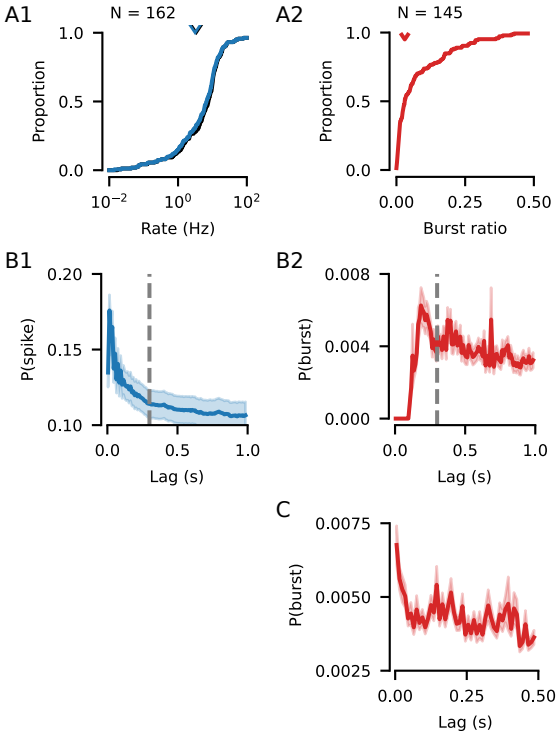

Figure S2 (A1) Distribution of firing rates (*black*) for all neurons recorded in spontaneous or sparse noise sessions (mean = 3.4 spk/s, N = 156). Neurons with a firing rate <0.01 spk/s were excluded from all analyses. The firing rate distribution considering only tonic spikes is shown in *blue* (mean = 3.1 spk/s), showing that overall firing rates are primarily determined by tonic spiking. **(A2)** Distribution of burst ratios (number of spikes assigned to a burst / total number of spikes, median = 3.0%). Bursts were detected in 89.5% of neurons. **(B1)** Mean auto-correlogram of tonic spiking (mean ± sem). The *dashed line* at 300 ms indicates the bin-width used to generate shuffled spike trains used to test phase coupling significance (see Methods). **(B2)** Mean auto-correlogram of bursting (mean ± sem). Note that the peaks are spaced apart by ∼ 200 ms, indicating that ∼ 5 Hz rhythmic bursting is present [see also 13]. **(C)** Mean burst cross-correlogram for all simultaneously recorded pairs of neurons (*highlighted region*: mean ± sem). The peaks at zero and ∼ 200 ms indicate that neurons tend to burst synchronously and rhythmically.

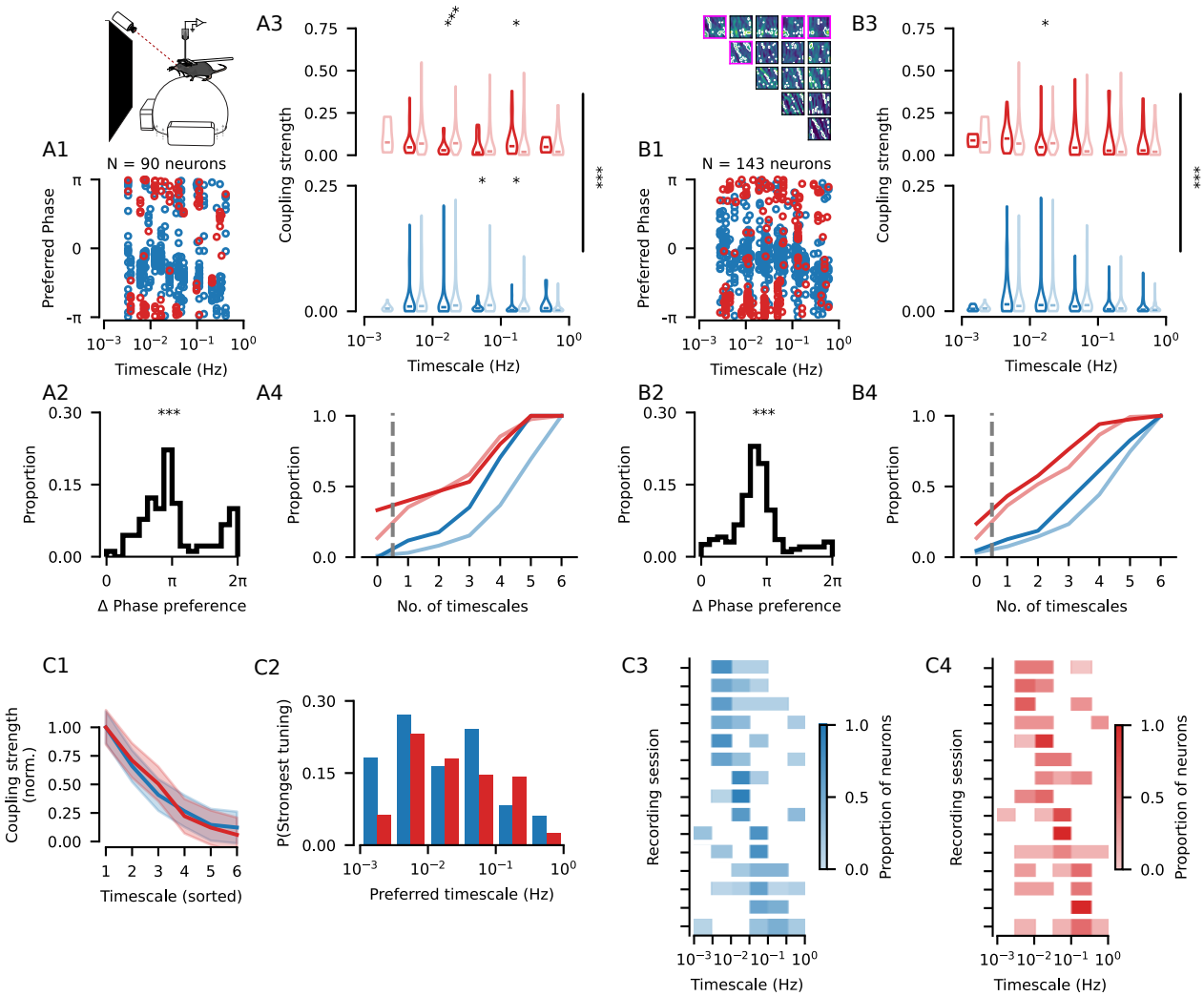

Figure S3 **(A)** Phase coupling analysis relating dLGN spiking to components of pupil dynamics (CPDs) for recordings performed in darkness. **(A1)** The preferred coupling phase of bursts (*red*) and tonic spikes (*blue*) for all neuron-CPD pairs with significant coupling (90/96 neurons showed significant coupling to at least one CPD). **(A2)** Distribution of the differences in preferred phase between bursts and tonic spikes from the same neurons (V-test for non-uniformity and a mean of π: V = 27.4, p = 2.2×10^{-5}). However, we also note that in darkness a substantial proportion of neurons appear to have a spiking pattern where tonic spikes immediately follow bursts without a phase delay (Δ phase preference $\approx 2\pi$). **(A3)** Coupling strengths binned by CPD timescale (*bold distributions*, *horizontal bars* denote median values). Burst spikes were more strongly coupled to pupil dynamics than tonic spikes (Wilcoxon rank-sum test pooling across timescales: W = 67.0, p = 1.6×10^{-15}). Across timescales, coupling strengths for neurons recorded in darkness were marginally lower than for neurons recorded in an illuminated setup (*faded distributions*, from Figure 2E; Mann-Whitney-U test for tonic spike coupling strengths pooled across timescales: U = 1.4×10^4, p = 0.05, Mann-Whitney-U test for burst coupling strengths pooled across timescales: U = 9.7×10^4, p = 4.1×10^{-3}), driven by changes at a few specific timescales (Mann-Whitney-U test for each timescale, p-value denoted by *asterisks*, * for p$\leq$0.05, ** for p$\leq$0.01, *** for p$\leq$0.001). **(A4)** Cumulative distribution of the number of CPDs to which each neuron was coupled from recordings in darkness (*bold lines*) compared to the distribution from neurons recorded in an illuminated setup (*faded lines*, from Figure 2F). As was the case for the recordings in Figure 2, more than half of neurons were significantly coupled to more than one CPD for both bursts and tonic spikes. **(B)** Phase coupling analysis performed on the same recordings as in Figure 2, but excluding spike that occurred during periods of phase coupling between CPDs (Figure S1D) **(B1)** Same as (A1). After exclusion of periods of phase coupling 92.0% (143/154) of dLGN neurons retained their coupling to at least one CPD for either bursts or tonic spikes. **(B2)** Same as (A2), tonic spikes and bursts tended to occur at opposing CPD phases (V-test for non-uniformity and mean of π: V = 90.3, p = 0.0), as was the case before removal of periods with phase coupling between CPDs (Figure 2D). **(B3)** Same as (A3). Bursts were more strongly tuned than tonics spikes (Wilcoxon rank-sum test: W = 1.4x$\times 10^3$, p = 3.7x$\times 10^{-25}$). There were no significant differences in coupling strengths for any timescale after periods of phase coupling between CPDs were removed (Mann-Whitney-U test: all p > 0.05). **(B4)** Same as (A4). Although neurons were on average coupled to fewer timescales after removal of periods of phase coupling between CPDs, the majority of neurons were still coupled to more than one CPD. *Continued on next page.*

Figure S3 *Continued from previous page.* **(C1)** Mean coupling strengths for tonic spikes (*blue*) and bursts (*red*) for neurons with coupling to more than one CPD (*shaded region*: mean ± SEM). Coupling strengths for each neuron were normalized to the neuron's highest coupling strength and sorted. **(C2)** The probability of observing a neuron with its strongest coupling in each of the timescale bins (i.e. the number of CPD-neuron pairs in a timescale bin representing the strongest coupling for that neuron normalized by the total number of CPD-neuron pairs in each bin for which coupling was evaluated). **(C3)** Distributions illustrating the proportion of neurons that have their strongest tonic spike coupling at each timescale for each recording session. The rows (sessions) are sorted by the timescale with the largest proportion of neurons. **(C4)** Same as (C2) but for bursts. For both tonic spikes and bursts, we generally observe that particularly strong coupling to each timescale is found in across multiple sessions (i.e. columns have more than one filled entry) and strong coupling can be found across multiple timescales within the recordings (i.e. rows have more than one filled entry). We note, however, that the preferred coupling timescale varies systematically between sessions (ANOVA for tonic spiking: $F = 3.1$, $p = 3.1 \times 10^{-4}$; ANOVA for bursting: $F = 4.2$, $p = 1.0 \times 10^{-5}$).

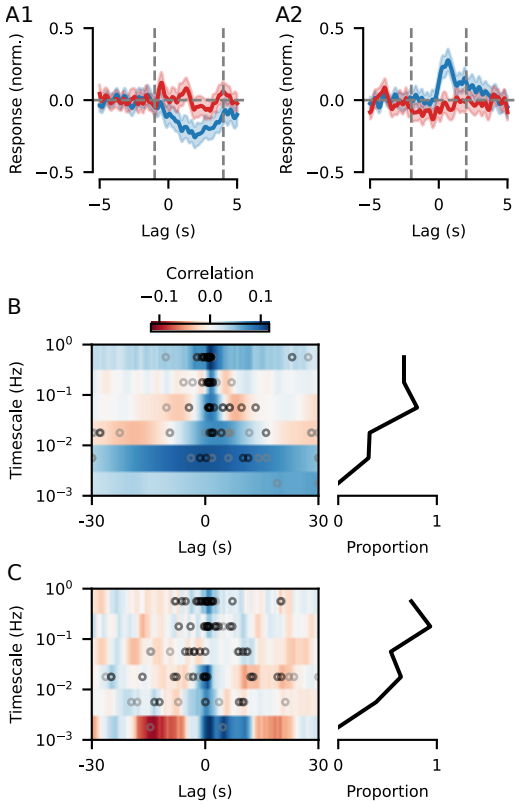

Figure S4 Spiking activity and pupil dynamics are correlated with locomotion speed. (A1) Mean firing rate activity across neurons (N = 121) at the offset of a running bout (firing rates were min-max normalized for each neuron; *shaded region*: mean ± sem; *horizontal line*: baseline firing rate defined as the mean rate from -5 to -3 seconds prior to the bout offset. The *vertical lines* denote the period surrounding the offset of running bouts during which the mean firing rate deviates from baseline (-1 s to 4 s), therefore spiking activity during this transition period was excluded for the analysis in Figure 4A, in addition to all activity during a running bout. **(A2)** Same as (A1) but for the onset of a running bout. The *vertical lines* denote the transition period (-2 s to 2 s) surrounding the onset of a running bout from which spiking activity was excluded for the analysis in Figure 4B, in addition to all activity during quiescence. **(B)** *Left*: Mean cross-correlation between components of pupil dynamics (CPDs) and locomotion speed, grouped by the timescale of the CPD (*black dots*: location of the peak correlation for each CPD with a significant correlation; *gray dots*: location of the peak correlation for each component without a significant correlation). Correlation significance was determined by comparing the maximum value of the cross-correlation to a null-distribution obtained by correlating the CPD with run speed traces taken from different recording sessions. To eliminate nonsense correlations, we only considered the cross-correlation significant if the peak was found at lags shorter than the mean period of each CPD. *Right*: Proportion of CPDs in each timescale bin with a significant correlation to locomotion speed. **(C)** Same as (B), but only considering the CPD and run speed *within* running bouts.

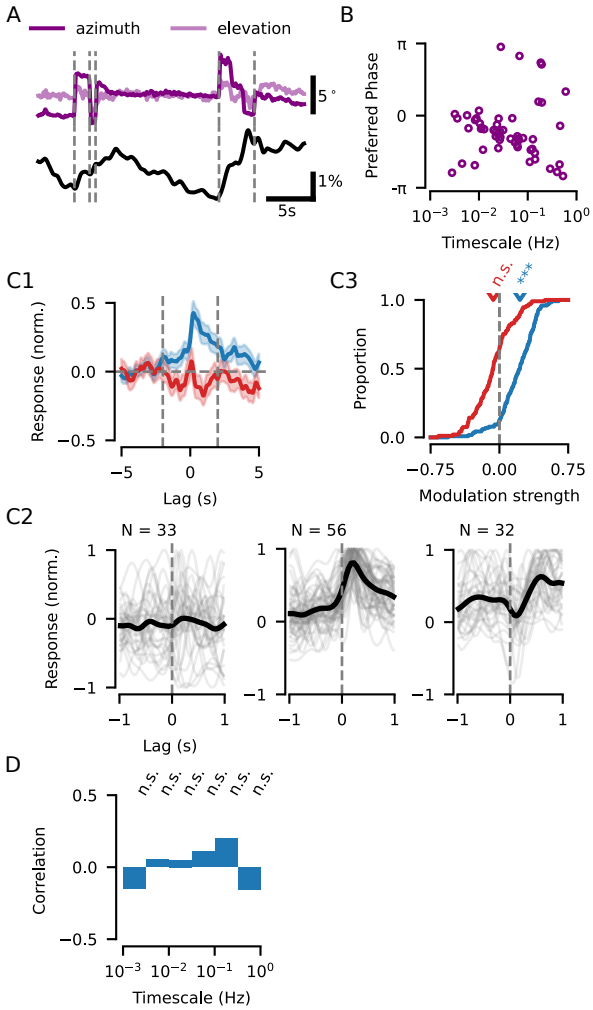

Figure S5 Saccades are linked to pupil dynamics and trigger changes in dLGN activity. (A) Example eye position (*top*) and pupil size (*bottom*) traces. Detected saccades are marked by the *dashed lines*. Note that saccades tend to occur during large slow dilations, and within these dilations saccades also appear to occur during the initial phase of a smaller dilations. **(B)** This coupling of saccades to pupil dynamics was verified using the same phase coupling analysis as in Figure 2, relating saccades to each of the components of pupil dynamics (CPD). Shown here are the preferred phases at which saccades occur, for CPDs across various timescales (significant saccade coupling to at least one CPD was observed in 15/15 recordings). Across all timescales, saccades tend to occur during pupil dilations, similar to tonic spikes (Figure 2C). **(C1)** Mean saccade triggered tonic spiking activity (min-max normalized) for all dLGN neurons (N = 121; *shaded region*: mean ± sem; *horizontal line*: baseline firing rate defined as the mean rate from -3 to -1 seconds prior to the saccade. The *vertical lines* denote the period surrounding the saccade during which the mean firing rate deviates from baseline (-1 s to 2 s), therefore spiking activity during this transition period was excluded for the analysis in Figure 4AC. **(C2)** Neurons in the dLGN have diverse saccade-triggered responses. Clustering the normalized peri-saccadic responses revealed at least two distinct response types, in addition to a minimally-responsive/ mixed cluster (*left*). The first responsive cluster (*middle*) had a transient increase in firing tightly locked to saccade onsets. The second responsive cluster (*right*) was characterized by gradually increased firing rates prior to saccade onset, with a brief suppression immediately following saccade onset, before returning to a sustained facilitation. **(C3)** Despite the diversity in responses, the peri-saccadic period (-2 to 2 s) was characterized by an overall increase in firing rates. This was quantified by taking the area under the normalized saccadic response curve in a window spanning -2 to 2 s (*modulation strength*) for 88% of neurons (N=121). The cumulative distribution shows that all responsive neurons had a positive modulation index, indicating an overall increase in firing relative to baseline. **(D)** For each temporal scale the CPD coupling strengths for tonic spikes were correlated with the neuron's saccadic modulation strength. The Pearson correlation was not significant for any timescale, suggesting that the coupling between tonic spiking and pupil dynamics was independent from the rapid peri-saccadic changes in firing rate observed in (C).

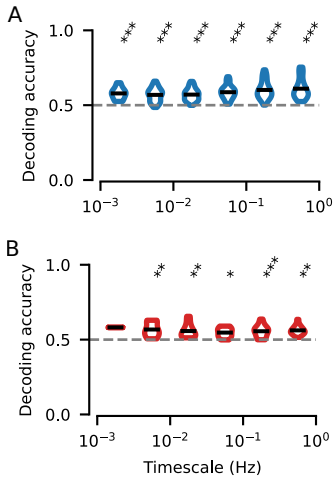

Figure S6 CPD phase can be decoded from spiking activity during stimulus viewing. (A) Distributions of decoding accuracy for predicting CPD phase from tonic spiking. For each neuron with significant tonic spike-CPD coupling, a support-vector classifier was trained to select between two phase bins, one of which was centered around the preferred phase of tonic spike coupling, the other was centered 180 deg opposite. Decoding accuracy was cross-validated using 5 training-test splits. The distribution of decoding accuracy was significantly greater than chance for all timescales (Wilcoxon rank-sum test for each timescale, p-value denoted by *asterisks*, * for $p \leq 0.05$, ** for $p \leq 0.01$, *** for $p \leq 0.001$) **(B)** Same as (A), but for predicting CPD phase from neurons with significant burst-CPD coupling. Support-vector classifiers were trained using bursting activity only, and the phase bins were centered around the preferred phase of bursting.